Hamburg University of Applied Sciences

Faculty of Life Sciences

The development of 3D X-ray imaging as a tool in the investigation of antibody-mediated kidney transplant rejection

Bachelor of Science

in the study program

Biotechnology

submitted by

Anna Kischlat

[redacted]

Hamburg,

the 3rd of December 2024

Reviewer: Prof. Dr. Jörg Andrä (HAW Hamburg)

Reviewer: Ph. D. Elizabeth Duke (EMBL)

The thesis was written in cooperation with the European Molecular Biology Laboratory (EMBL), Hamburg.

This thesis is dedicated to the memory of my father, Oliver Hans Kischlat (1963 - 2017).

Table of Contents

I. List of Abbreviations

2D	-	two-dimensional
3D	-	three-dimensional
AMR	-	antibody-mediated rejection
BM	-	basement membrane
CT	-	computed tomography
DESY	-	Deutsches Elektronen Synchrotron
DESY II	-	Deutsches Elektronen Synchrotron II
DSA	-	donor-specific antibodied
DSAneg	-	donor-specific antibody negative
EM	-	electron microscopy
EMBL	-	European Molecular Biology Laboratory
ESRF	-	European Synchrotron Radiation Facility
H&E staining	-	haematoxylin and eosin staining
HLA	-	human leukocyte antigen
IF	-	immunofluorescence
IHC	-	immunohistochemistry
LINAC II	-	Linear Accelerator II
linac	-	linear accelerator
MAC	-	membrane attack complex
MARVIN	-	MultiAxesRoboticVersatileINstaller
MHC	-	major histocompatibility complex
MoBIE	-	MultiModal Big Image Data Sharing and Exploration

NK cells	-	natural killer cells
PETRA III	-	Positron-Elektron-Tandem-Ring-Anlage
PFA	-	paraformaldehyde
PIA	-	Positronen-Intensitäts-Akkumulator
RF	-	radio frequency

II. List of Tables

III. List of Figures

1. Abstract

The aim of this thesis was to gain a better understanding of the effects of antibody-mediated rejection (AMR), focusing on the glomeruli of kidney transplant recipients. AMR is one of the leading causes of graft loss after an organ transplantation. To collect data, a three-dimensional (3D) imaging technique called holotomography is used to image kidney punch biopsies, taking advantage of the high coherence of X-rays produced by the Deutsches Elektronen Synchrotron (DESY). Data from 79 glomeruli across six patients was collected, focusing on characteristics such as their volume, surface area and sphericity. A correlation was found between a patient's AMR stage and the health status of the investigated glomeruli. In addition, the change in the volume and surface area of globally sclerosed glomeruli compared to healthy and segmentally sclerosed glomeruli was statistically analysed, highlighting the correlation between volume/surface area and the health status of a glomerulus. The plausibility of the results could be confirmed by other studies. However, it must be considered that only a very small random sample was analysed. In order to obtain reliable results, the investigations undertaken here would have to be repeated on a larger scale. It would be important to consider other factors influencing the size of the glomeruli, such as the demographics of a patient. This work underscores the potential of 3D imaging to enhance understanding of AMR's impact and improve diagnostic strategies.

2. Introduction

To this day, kidney transplantation is the most favourable treatment for patients with end-stage renal disease, offering a higher survival rate than dialysis and improving the quality of life significantly[1]. In 2022, more than 100,000 kidney transplants were performed worldwide[2]. However, the success of a kidney transplant is not guaranteed. One of the biggest challenges is the immune system's response to the transplanted organ. Rejection occurs in up to 10% of all kidney transplants[3]. There are several reasons why a recipient may reject a transplant. These include cellular rejection and antibody-mediated rejection (AMR), the latter of which is less common and the focus of this thesis[4]. AMR is an immunological process that occurs when the recipient recognises the transplanted organ as foreign and attacks it with antibodies[5,6]. As the disease progresses, other immune cells, such as natural killer (NK) and T cells, are activated. AMR can damage the kidney transplant, jeopardising both graft function and patient survival[7,8]. Additional complications arise from the fact that chronic AMR can occur months or even years after the surgery. Therefore, the patient cannot receive immediate help. In cases of hyperacute and acute AMR, the patient is still under close medical observation and can be treated more quickly[3,9]. Currently, there is no universally applicable way to treat AMR. Due to ineffective treatment with immunosuppressive drugs, up to 30% of patients who experience AMR face graft loss in the first year after transplantation[3].

Therefore, there is a great need to better understand how AMR works and how it affects the functionality of the graft. Currently, there are several ways to study AMR in renal pathology. Hospitals rely on a combination of diagnostic approaches to identify AMR. The methods routinely used are histological analyses, such as haematoxylin and eosin (H&E) staining, electron microscopy (EM), immunohistochemistry (IHC) and immunofluorescence (IF)[9,10]. The information obtained and collected by these methods is two-dimensional (2D) and, thereby, does not provide a holistic picture of the effect of AMR on the graft[11].

To investigate the effect of AMR on a kidney transplant, this thesis focuses on a method of three-dimensional (3D) X-ray imaging using X-rays generated by the Deutsches Elektronen Synchrotron (DESY) in Hamburg, Germany. The thesis provides an overview of the current state of science as well as the limitations and strengths of current diagnostic techniques for investigating AMR in kidney transplants. A case study of 79 glomeruli identified from six kidney biopsies from different patients is presented. Four with AMR and two patients with non-AMR renal health issues which are used as negative controls to demonstrate the benefits of 3D X-ray imaging.

This research aims to contribute to better diagnostic practice and more successful long-term kidney transplant outcomes by improving the understanding of AMR.

3. Theoretical Background

To illustrate the importance of the new method and to provide a context for understanding its implications, an overview of the current state of science on AMR and the methods used to study its impact is given.

3.1. Kidney anatomy and function

The kidneys are bean-shaped organs located in the rear abdomen. The average healthy person has two kidneys, which are a vital part of the urinary system. Their primary function is to filter blood. The pollutants are excreted in the form of urine. Not only do they remove toxins from the bloodstream, but they are also responsible for maintaining the fluid/electrolyte balance[12,13].

In general, the anatomy of the kidneys can be divided into two different sections. The outer cortex is where the nephrons are primarily located, and the renal medulla is the kidneys' inner part. The medulla consists of parallel tubules and small blood vessels. Furthermore, the medulla is made up of several cone-shaped renal lobes surrounded by the cortex. These are called renal pyramids. At the tip of the renal pyramids, the excreted urine exits the medulla through capillary-like structures that feed into the ureter. At the hilum, where both the ureter and the renal vein exit the kidney, the renal artery enters[13].

The schematic structure of a kidney can be seen in **Figure 1**.

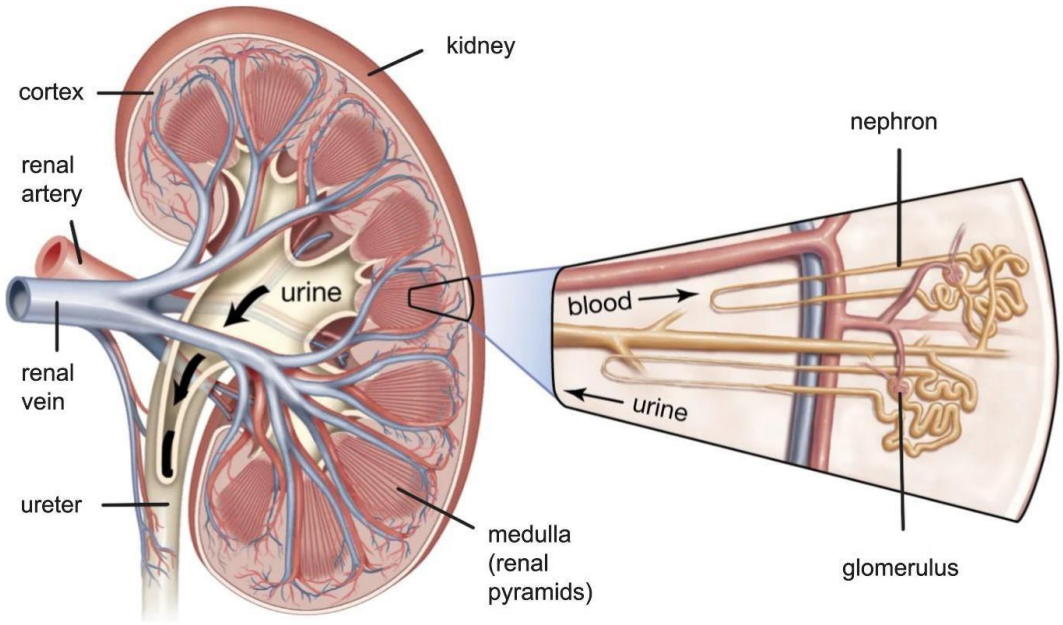

Figure 1: Cross-section of a kidney and a close-up look showing a nephron and a glomerulus[14] (edited picture)
On the left, the renal artery enters as the ureter and the renal vein exit the kidney. The cortex and the medulla are indicated.
On the right, a close-up of a nephron, a glomerulus, and the renal tubules, which partially extend into the medulla, are shown.

The actual filtration takes place in the nephrons. A nephron consists of a renal tubule and a renal corpuscle comprising a glomerulus, the Bowman's capsule, and the Bowman's space. Nephrons can be divided into cortical and juxtamedullary nephrons that differ in structure. The tubules of cortical nephrons are mainly located in the cortex and only reach the outer medulla. Whereas the tubules of juxtamedullary nephrons reach far into the medulla[15].

This paper will focus on the function of the glomeruli and the filtering steps within them. Glomeruli are tufts of capillaries encapsulated by the Bowman's capsule. The capillaries inside the glomeruli are one of the key factors for a high renal ultrafiltration rate. The large number of small capillaries inside the Bowman's capsule creates a large filtration area. Here, a filtrate is produced, which is further processed by the renal tubules to produce urine. The constriction differences between the afferent and the efferent arteriole create the needed pressure for this ultrafiltration. The former transports the polluted blood into the glomerulus, while the latter transports the filtered blood out of the glomerulus[15].

The permeability of the capillaries in the glomerulus is highly selective. This ensures that only the unwanted substances are filtered out. The highly selective filtration barrier consists of three key components. Thin endothelial cells form the inner wall of the tuft. These are covered by the basement membrane (BM), a collagen-rich membrane consisting of negatively charged proteoglycans that extend well beyond the glomerulus and cover the tubule of a nephron. The last notable component is the podocytes. The podocytes, like the BM, are covered with negatively charged glycolyzed macroproteins. The negative net charge repels similarly charged molecules such as albumin. This characteristic ensures that only a minimal amount of small negatively charged molecules are lost, which would otherwise be able to pass the permeable membrane due to their size. The efficiency is highlighted by the fact that only about 30 mg of albumin is lost, compared to the estimated amount of 35 g that passes through the kidney's filtration units every day (assuming a renal plasma flow of 600 mL/min and an albumin concentration of 40 g/L)[15].

3.2. Antibody-mediated rejection

Antibodies are an important part of the immune system. They are responsible for recognising foreign structures, which enables the body to fight pathogens at an early stage[16]. Unfortunately, the foreign structures recognised by the antibodies are not necessarily pathogenic. A transplanted organ may be categorised as foreign and potentially pathogenic by the recipient's donor-specific antibodies (DSA). Triggering an immune response, in many cases, leading to transplant rejection and, in the long run, graft loss[8]. AMR can be divided into three different types: hyperacute, acute and chronic AMR. Hyperacute AMR used to be a very serious complication caused by pre-existing DSA, leading to graft rejection minutes to hours after the completion of the surgery. Nowadays, ABO antigen testing and other tissue typing methods are performed, which significantly reduces the risk of hyperacute AMR. Acute AMR and its associated histological features are very similar to hyperacute AMR. The main difference is the time it takes to develop. Acute AMR usually occurs days to weeks after the transplantation and occurs in up to 7% of all kidney transplant recipients. In chronic AMR, DSA slowly activate the complement system and gradually causes damage to the allograft, a process that can take many years and often leads to chronic graft dysfunction[3,9].

In **Figure 2** the immune cells involved in an AMR and the basic steps in the rejection process are illustrated.

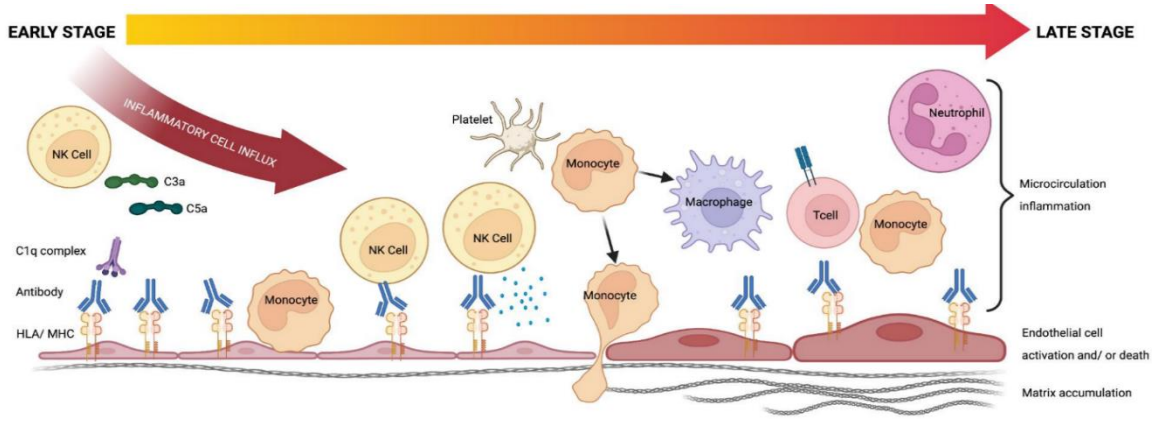

Figure 2: Progression of AMR, the different stages of the disease and the involved immune cells[17] (edited picture)
After DSA recognise the endothelial cells of the graft as foreign, a complement immune response is activated, including NK cells, monocytes and other relevant immune cells like macrophages.
AMR – antibody-mediated rejection, DSA – donor-specific antibodies, NK cells – natural killer cells

DSA in the recipient's blood bind to the surface of the organ's endothelial cells because the antigens on the grafts' surface are recognised as foreign. They primarily bind to the human leukocyte antigen (HLA) system, also known as the human major histocompatibility complex (MHC). The binding of DSA to the HLA is classified as an adaptive immune response, which in turn initiates the classical complement pathway of the immune system as C1q binds to the antigen-antibody complex. The activated complement cascade produces C3 convertases, which generate C3a, C5a and C3b fragments. C3a and C5a fragments attract phagocytes, such as monocytes, to the graft surface, whereas C3b marks the endothelial cells of the graft for phagocytosis. When C3b binds to the C3 convertase, the C5 convertase originates, causing C5a and C5b fragments to be produced by splitting the complement component 5. C5a is a potent anaphylatoxin with chemotactic properties activating NK cells. NK cell cytotoxicity against the graft tissue is enhanced, and more pro-inflammatory cytokines are released, further amplifying the immune response. Activated monocytes initiate phagocytosis of opsonised debris from injured graft cells. At the same time, C5b activates the formation of the membrane attack complex (MAC). The MAC penetrates the endothelial cells of the transplanted organ and causes cell lysis.

This leads to cell debris being released, which attracts NK cells, monocytes, and platelets. Platelets are activated by C5a and adhere to the subendothelial matrix exposed by cell lysis, causing ischemia of the allograft. In later stages of AMR, neutrophils, T cells, and monocytes that differentiate into macrophages play a critical role. Enzymes released by neutrophils intensify the tissue injury, while macrophages continue to phagocytise cellular debris and release more pro-inflammatory cytokines, further amplifying the inflammation. In response to the cytokines and tissue damage, T cells are activated. Collectively, all these processes lead to continuous tissue injury, thrombosis and potentially the complete loss of graft function[16].

3.3. Current methods in renal pathology for diagnosing antibody-mediated rejection

Currently, hospitals use a variety of histological analyses to diagnose AMR. Histology is the study of structures in plant and animal tissues under a microscope[18]. The term histopathology is used to describe the study of diseased tissue and the manifestation of a disease in tissue[19]. The most commonly employed histopathological method in hospitals is H&E staining. In this method, two histological stains, namely haematoxylin and eosin, are combined. Haematoxylin stains the nuclei of the cells a blue-to-purplish shade, while the extracellular matrix and cytoplasm are stained pink by eosin. Other structures might be stained by both substances, leading these structures to take on different shades and combinations of these colours[20]. IHC uses the specificity of antigen-antibody interactions. Enzyme labels are visualised by exposure to specific substrates, resulting in the amplification of tissue structures. Different protocols are available for direct and indirect staining[21]. Like IHC, IF also relies on antigen-antibody interactions. In this case, fluorescent labels are used to visualise the tissue structures. There are two types of IF: direct and indirect. The former only uses one fluorescent labelled antibody, while the latter uses an additional secondary antibody to amplify the signal[21].

Representative images acquired by these techniques can be seen in **Figure 3**.

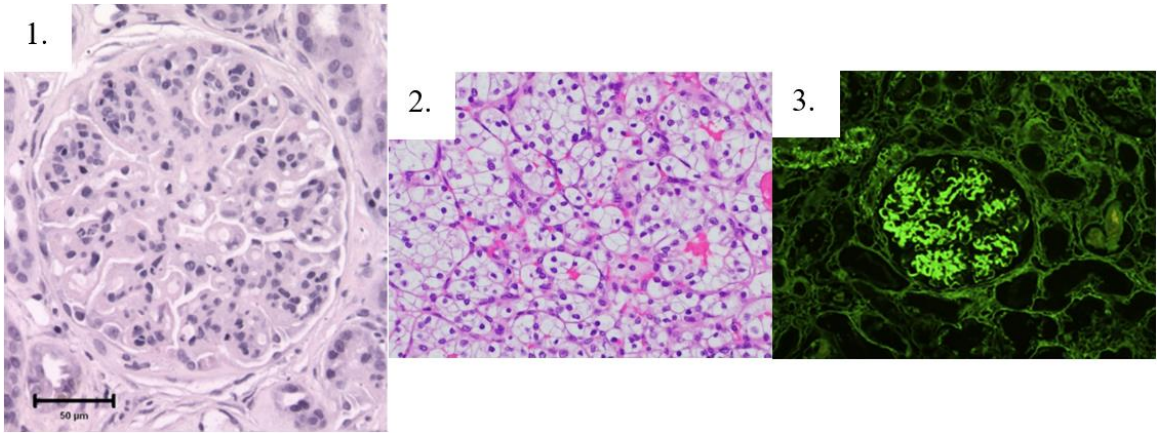

Figure 3: Comparison between images obtained by H&E staining (1.), IHC (2.) and IF (3.)
1. Staining of a glomerulus[22]
2. Antibody staining of a clear cell renal cell carcinoma[23]
3. Segmental glomerular capillary wall staining[24]
H&E staining – haematoxylin and eosin staining, IHC – immunohistochemistry, IF - immunofluorescence

One significant benefit of H&E is the durability of the staining. Furthermore, it is easy to interpret, cost-efficient and can be employed for a range of tissue types from diverse specimens. The versatility of H&E staining is accompanied by a lack of specificity in detecting and visualising subtle changes in tissue morphology. A further limitation is the subjective interpretation of the stained structures and the information lost through the analysis of a few 2D sections of a 3D structure[25]. The advantages of IHC include long-lasting staining, providing a permanent record, and broad compatibility with all routine histological specimens, resulting in its crucial role in diagnostic pathology. Low resolution and the inability to perform multi-colour staining are the main limitations of IHC. In contrast to IHC, the strengths of IF lie precisely in these areas, i.e., the ability to perform multi-colour staining and the acquisition of high-resolution images. However, like any other method, IF has its limitations, such as a phenomenon called photobleaching, which describes the fading of the fluorophores over time and the expensive equipment required. The generated images from both techniques share the limitation of providing only 2D information[21].

In EM, the illuminating radiation is not visible light but electrons. Resulting in a resolution 1,000 times more detailed than the resolution of light microscopy[26]. Allowing detailed structures of tissues, cells, organelles, and macromolecular complexes to be studied, particularly the effects of disease on these structures.

EM can be divided into two main types. The first is transmission EM, in which thin slices of tissue can be passed through by electrons, which then produce projection images. To enhance the contrast achieved by this method, the tissue slices must be stained with heavy metals like lead[27,26]. Secondly, scanning EM, where the back-scattered electrons are recorded[26]. An example of transmission and scanning EM images is shown in **Figure 4**.

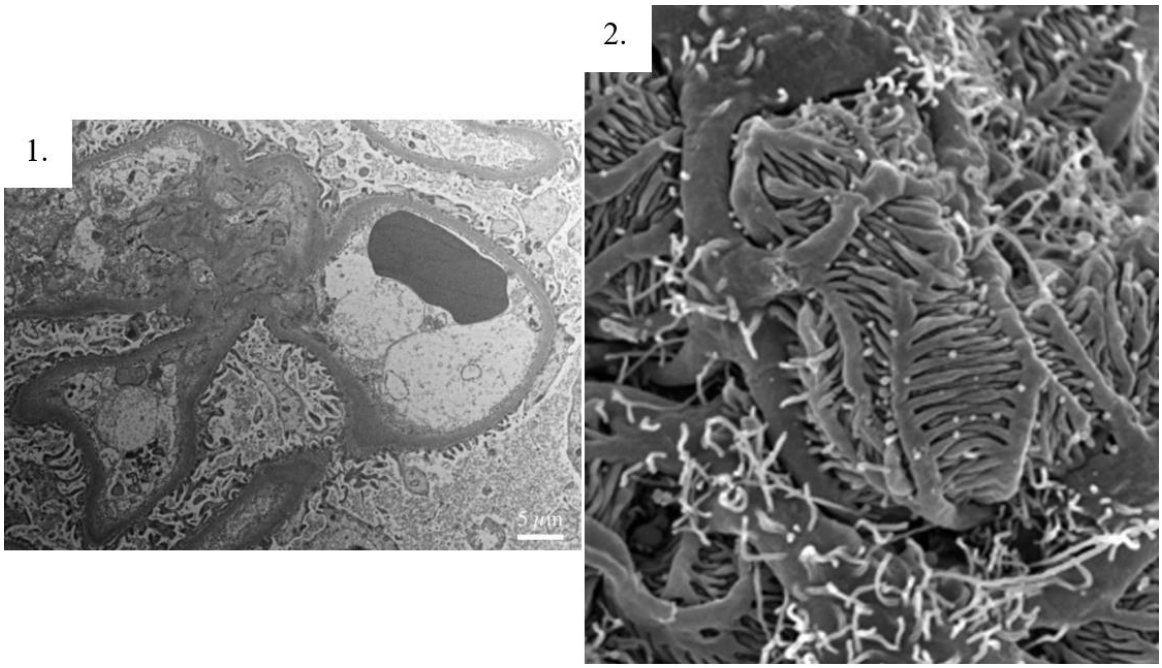

Figure 4: Images acquired by transmission EM (1.) and scanning EM (2.)
1. Image of a normal peripheral capillary loop covered by intact podocyte foot processes[28]
2. Image of renal podocytes[29]
EM – electron microscopy

The main advantages of EM, besides the achievable resolution of 0.2 nm in cryogenic EM and 1-10 nm in general, are the diverse applications in many different fields of research, such as chemistry, biomedicine and quality control in materials science, as well as its ability to produce highly detailed images of complex structures that other histological techniques cannot reproduce. Disadvantages of EM include long acquisition times, depending on the number of areas and the desired details, the need for a vacuum, which precludes the analysis of live specimens, the fact that only 2D images can be produced and the expensive equipment[30].

3.4. X-rays

Discovered in 1895 by the German physicist Wilhelm Conrad Röntgen, X-rays are a form of electromagnetic radiation. In contrast to visible light, X-rays have a higher energy. Due to the higher energy, X-rays can penetrate the tissues of the human body. Röntgen first visualised them using screens coated with barium platinocyanide. On these fluorescent screens, the unknown radiation produced shadows of different shades of grey depending on the degrees of transparency and density of the passed material, as illustrated in **Figure 5**[31,32].

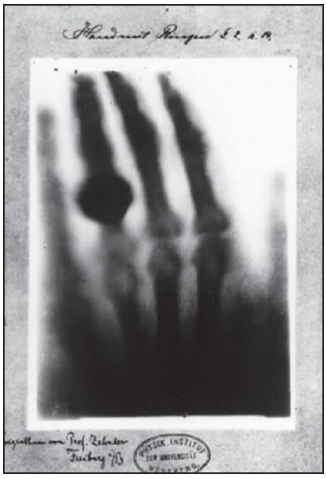

Figure 5: X-ray of the left hand of Röntgen's wife, Anna Bertha Ludwig, on a photographic film in 1896[31]

For the first time, doctors were able to visualise internal structures without invasive procedures. X-rays are absorbed in varying amounts by different types of tissue and human bone, depending on their radiological density, which is equal to their electron density. Traditionally, the contrasts in absorption are visualised by an X-ray detector, producing a negative image. The radiographs shade changes according to the amount of radiation it receives. Less radiation can pass through denser objects, so these structures appear lighter, almost white, on modern medical radiographs. Bones, for example, contain calcium, which absorbs more X-rays, resulting in bones appearing white on radiographs. Soft, less dense tissues, such as muscle, fat, and the air-filled lungs, allow more radiation to pass through, resulting in shades of grey on the radiograph. Today, X-rays are routinely used to identify internal features such as fractures, certain tumours, and other abnormalities, such as pneumonia[32].

After learning about the interactions between X-rays and human tissue and how they are used in modern medicine, it is explained how X-rays are produced. X-rays are produced when electrons are accelerated under a high potential difference and converted into electromagnetic radiation. These range higher in the electromagnetic spectrum than ultraviolet light and lower than gamma rays, which allows X-rays to penetrate tissue. The components of an X-ray tube include two electrodes, a cathode, an anode, and a vacuum enclosure. A schematic diagram is shown in **Figure 6**[32–34].

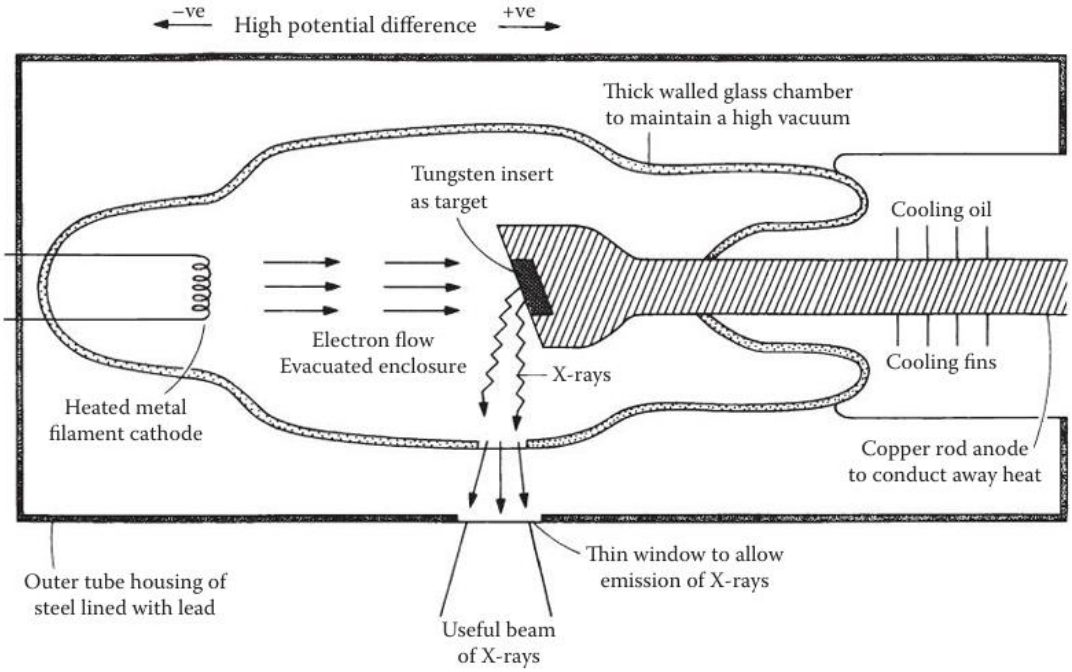

Figure 6: Features and simplified function of an X-ray tube[34]

In the generation of X-rays, a cathode filament is heated. This causes the filament to release electrons in a process called thermionic emission – a cloud of electrons forms at the filament surface. By applying a high voltage to the electrodes, the emitted electrons are accelerated in the direction of the anode. At the anode, the electrons collide with the anode target, typically consisting of tungsten, which is a very dense and heavy element that the electrons cannot penetrate. The sudden deceleration causes X-ray photons to be emitted. The emitted X-rays are made useable by a thin window through which the beams can pass. The resulting electron kinetic energy (measured in keV) depends on the applied voltage[33,34].

In computed tomography (CT), conventional X-ray technology produces cross-sectional 2D images or so-called slices. In medical CT, the X-ray source and the detector are rotated around the patient to collect information from different angles. Once the desired number of slices has been acquired, a complex computer program is used to stack the different slices and create a 3D view of internal structures such as organs and possible abnormalities. These developments are benefiting many different areas of medicine, including oncology, cardiology, and trauma care[32,35].

X-rays nowadays are an indispensable part of medical diagnosis. But they do not come without risks. The ionising radiation emitted can increase the risk of developing cancer if patients are exposed to it too often. Furthermore, it has the potential to cause significant damage to living tissue. For this reason, there are various restrictions on the use of X-rays in medicine, particularly regarding the dose of radiation to which patients are exposed to. Vulnerable groups such as pregnant women are advised to avoid X-rays because of the potential negative impact on embryonic development. Where possible, other techniques, such as ultrasound or magnetic resonance imaging, should be used instead. In addition to the restrictions, scientists are focusing on developing technologies such as digital detectors to maintain or improve the image quality while reducing the amount of radiation[36].

3.4.1. Deutsches Elektronen Synchrotron

The synchrotron DESY is located in Hamburg. All synchrotron radiation sources are storage rings such as the Positron-Elektron-Tandem-Ring-Anlage III (PETRA III) at DESY, where the charged particles, typically electrons, are accelerated and kept on a circular path by bending magnets[37].

The layout of some of the relevant facilities on the DESY campus is shown in **Figure 7**.

Figure 7: A look at the layout of the DESY campus[38] (edited picture)
DESY – Deutsches Elektronen Synchrotron

Before the electrons enter the PETRA III storage ring, they must be pre-accelerated. The pre-acceleration takes place in three different steps. These steps take place in the Linear Accelerator II (LINAC II), the Positronen-Intensitäts-Akkumulator (PIA) and Deutsches Elektronen Synchrotron II (DESY II). Before the electrons are accelerated in LINAC II, they must be produced by an electron gun. This process is similar to the generation of X-rays in an X-ray tube. A negatively charged metal, which acts as the cathode, is heated, causing electrons to be emitted. While the electrons are accelerated in the direction of the anode, the beam is focused by a collimator. The anode is a positively charged ring of metal. The electrons are then guided through the anode by its electrostatic field towards the prebuncher. Here, the electron beam is split into bunches with a length of 0.3 ns. The electron bunches then enter the linear accelerator (linac) and are accelerated. A klystron is used to synchronise the movement of the electron bunches with the radiation so that the bunches are always located in a field whose orientation increases their energy.

The klystron also plays a crucial role in keeping the electron bunches compact[39]. The layout of the electron gun, the klystron and the linac is shown in **Figure 8**.

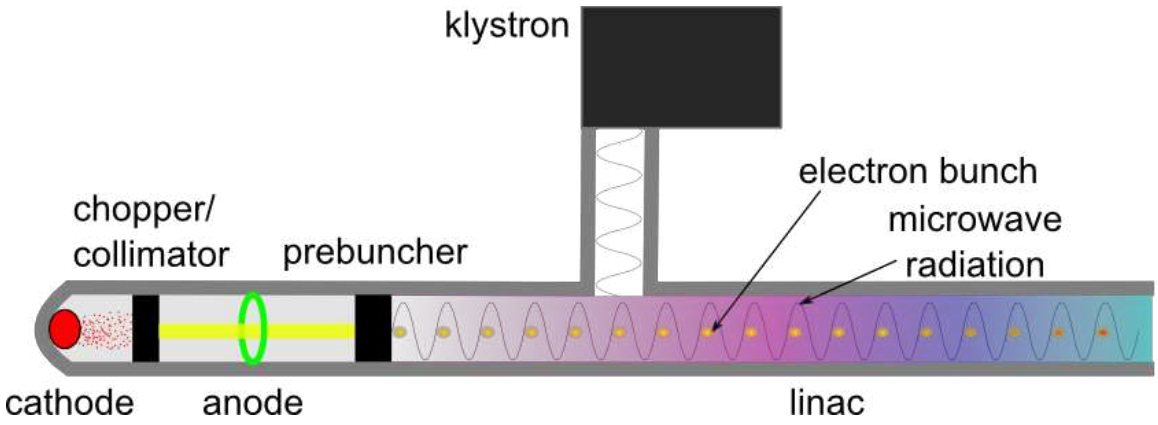

Figure 8: A simplified overview of the setup for the pre-acceleration steps[39]
linac – linear accelerator

Once the electron bunches leave LINAC II, they travel at close to the speed of light. Before entering PETRA III, the electrons pass through two booster synchrotrons to reach their final speed and energy of 6 GeV[39,40]. In the two booster synchrotrons PIA and DESY II, the electrons receive a boost from a radio-frequency (RF) system similar to the one in the linac, consisting of a klystron, waveguides and RF cavities. Before entering PETRA III, the electrons have a speed of 99.9999993% of the speed of light[39]. It, therefore, takes the electron bunches 7.7 µs to travel around the 2304 m long storage ring. The electrons travel through an ultra-high vacuum to allow the electron bunches to circumnavigate the storage ring for several hours. Strong magnetic fields generated by bending magnets force them to stay on a circular path. As the accelerated electrons move around the arc, they emit a small beam of radiation. This is one of the sources of radiation, along with wigglers and undulators[39].

The structure of the PETRA III tunnel is shown in **Figure 9**.

Figure 9: PETRA III tunnel (picture provided by Jonas Albers)
On the right-hand side is the vacuum tube through which the accelerated electrons move. Bending magnets, red, and undulators, yellow, keep the electron bunches on their circular pathway, causing radiation to be emitted.

Wigglers produce the same type of radiation as bending magnets, but the intensity of the radiation is increased in proportion to the number of magnet poles. The electrons are forced to zigzag, resulting in the emission of radiation. Undulators use weaker magnetic fields, and smaller magnets are used, resulting in shorter periodic undulations. The short periods cause the beams generated to overlap. This interference gives the radiation special properties. After passing through the undulator, the beam is directed into a beamline, where the experiments take place[39]. A monochromator can filter out a particular wavelength of the beam's spectrum to produce a monochromatic beam of the desired energy, thereby tuning the properties of the radiation to the requirements of different experiments. The resulting beam is monochromatic. Other facilities use white and pink beams where no wavelengths or only a small range is filtered out. Beamline P14 uses a double-crystal Si(111) monochromator. The first crystal filters out the wavelength of interest, and the second redirects the radiation in a straight line. The radiation beam exits the vacuum tube through an artificial diamond window, allowing the radiation to be used for experiments while maintaining the vacuum and protecting the vacuum tube from contamination.

The X-ray imaging setup at P14 consists of a rotation and translation stage for the samples (Arinax MD3), a sample mounting system, MultiAxesRoboticVersatileINstaller, called MARVIN, and an X-ray microscope, as well as several computers to correct and reconstruct the acquired data[41]. The path of the X-rays at P14 is shown schematically in **Figure 10**.

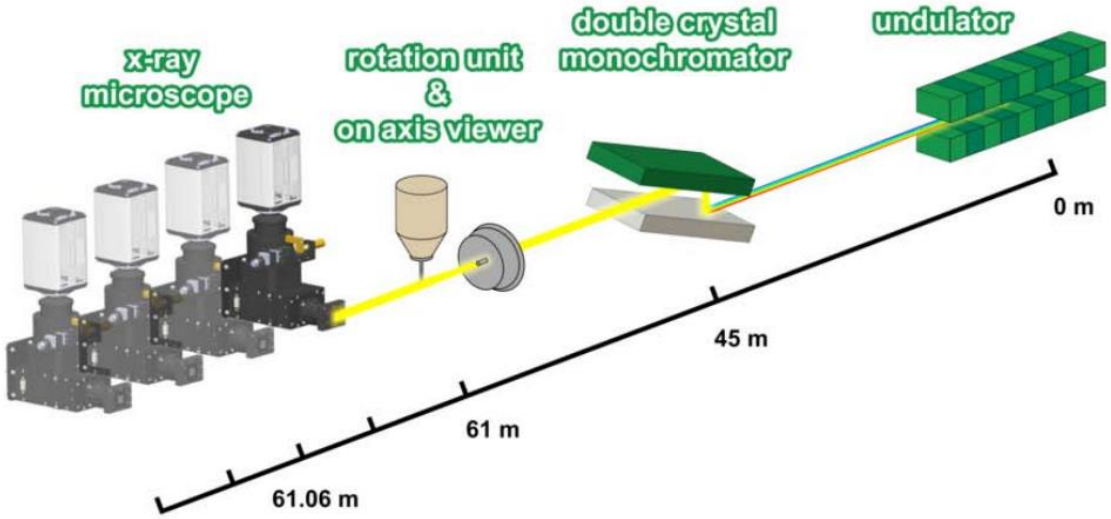

Figure 10: Schematic setup of P14[41] (edited picture)
The EMBL beamline P14 consists of an undulator generating the polychromatic X-ray beam. The double-crystal Si(111) monochromator filters out all unwanted wavelengths creating a monochromatic X-ray beam. The monochromatic X-ray beam is targeted at the sample, which is mounted on the rotation unit. Imaging data is collected with a special X-ray microscope.
EMBL – European Molecular Biology Laboratory

3.4.2. Phase contrast three-dimensional X-ray imaging

In hospitals, absorption-based X-ray imaging is used to locate fractures. However, this method can only be used if the elements in the sample vary significantly in their atomic number. Because the attenuation of X-rays by soft biological tissues is relatively weak, absorption-based X-ray imaging alone cannot reveal their internal structures. Fortunately, this is not the only property of X-rays affected by passing through a material. Like visible light shining through a glass window, X-rays can be refracted. Refraction causes a change in the phase of the X-ray beam[42]. However, X-ray detectors are not able to visualise the shift in phase directly, but through the interference of the wavefront between the sample and the detector.

The phase shift causes intensity variations, which in return can be measured by commercial X-ray detectors[41], as shown in **Figure 11**. For this effect to be measured, a coherent and brilliant radiation source like a synchrotron is needed.

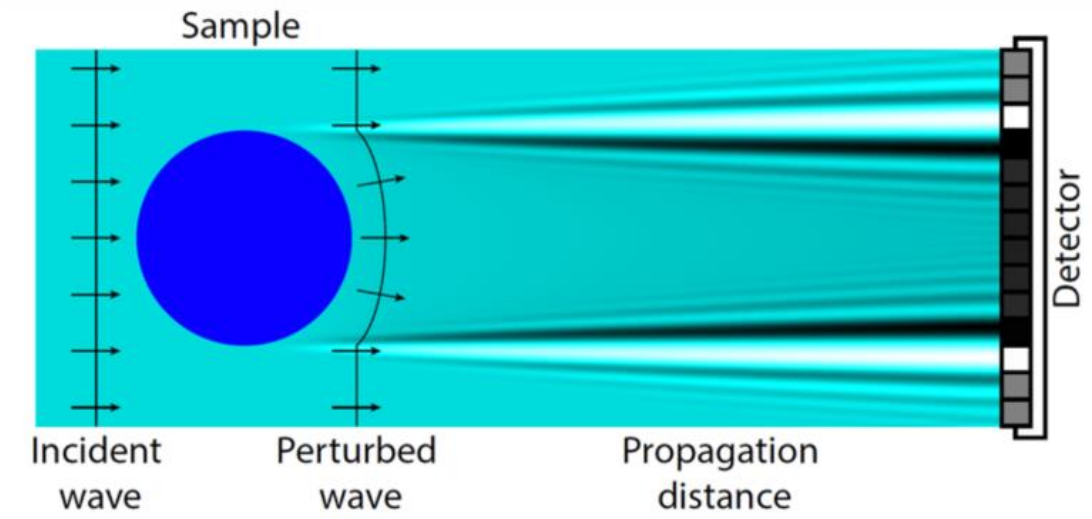

Figure 11: Schematic look at the occurring intensity variations at the detector in propagation-based X-ray imaging[43]

There are various phase contrast techniques such as the Bonse–Hart interferometer, analyser-based phase-contrast imaging, Zernike phase contrast based on Fresnel lens optics, grating-based methods, and propagation-based phase contrast. Here propagation-based phase contrast is used because, in comparison to all other methods, it is the only method that does not rely on any special optical elements[42].

When propagation-based X-ray imaging is combined with the technique behind CT, it is possible to reconstruct a 3D image based on the recorded projection images[44]. There are two different methods of propagation-based X-ray imaging. One is edge detection, and the other is holographic phase contrast. In edge detection, also known as direct-contrast regime, a tomographic dataset is acquired at a single, relatively small propagation distance. This results in projections with strong edge contrast because the diffraction is reduced to edge enhancement, but the original image can still be seen. This method is widely used. In holographic phase contrast, the sample is typically measured at four different propagation distances. Each distance is sensitive to a particular range of spatial frequencies. Longer propagation distances are required compared to edge detection. This allows multiple oscillatory variations (fringes) to be observed[45]. In this work, holographic phase contrast (holotomography) was used, because the imaging setup at beamline P14 does not support the needed propagation distance for edge detection.

4. Materials

In this thesis, different hardware and software were used (**Table 1** & **Table 2**) to process the acquired data.

Table 1: Manufacturer and name of the hardware used during this work

Manufacturer	Name	Model identifier	Specification
Dell	Intel core i9	10980xe	256 GB RAM
Nvidia	RTX A5000	VCNRTXA5000-PB	-
Wacom	Cintiq 22	DTK2260K0A	-

Table 2: Developer and name of the used software
EMBL – European Molecular Biology Laboratory, ESRF – European Synchrotron Radiation Facility

Developer	Name
Pape *et al.*[46]	MultiModal Big Image Data Sharing and Exploration (MoBIE)
Thermo Fischer Scientific	Amira™ 3D
European Synchrotron Radiation Facility (ESRF)	MXCuBE
Paul Scherrer Institute	NRStitcher
Duke Team (European Molecular Biology Laboratory (EMBL) Hamburg)	TOMO CTF
Gürsoy *et al.*[47]	TomoPy
Microsoft	Excel

Materials used to prepare the biopsy samples in the UK are not listed. A summary of the used biopsies and their disease state can be found in **Table 3**. The identifiers are pseudonymised to conceal the identity of the patients.

Table 3: The identifying number and the disease state of all examined kidney biopsies
AMR-high datasets show severe signs of AMR in a later stage of the disease.
AMR-low datasets show signs of an early-stage AMR.
DSA negative (DSAneg) biopsies show no signs of DSA and are therefore classified as DSAneg.
AMR – antibody-mediated rejection, DSA – donor-specific antibodies, DSAneg – donor-specific antibody negative

Biopsy identifier	Disease state
EM04596_2	AMR-high
EM04628	AMR-low
EM04633_2	DSAneg
EM04639_1	DSAneg
EM04657_2	AMR-low
EM04691_2	AMR-high

Specifications of the technical equipment used to acquire the data are listed in **Table 4**.

Table 4: Technical equipment of the beamline P14
EMBL – European Molecular Biology Laboratory, ESRF – European Synchrotron Radiation Facility, MARVIN – MultiAxesRoboticVersatileINstaller

Manufacturer	Name	Specification
DESY	U29 undulator	source size 13 µm and 330 µm
EMBL Hamburg	double-crystal Si(111) monochromator	6 keV – 30 keV
Arinax	MD3 diffractometer	-
Optique Peter	monochromatic X-ray beam imaging microscope	660 nm / 330 nm
ESRF	LSO:Tb scintillator	8 µm active layer
Olympus	UPlanFL 20-fold objective lense	-
PCO	PCO.edge 4.2 sCOMS camera	2048x2048 pixel sensor, pixel size 6.5 µm, effective pixel size 0.325 µm resulting in a 666 µm x 666 µm field of view
MiTeGen	Magnetic goniometer bases	-
EMBL Hamburg	MARVIN	-
-	Spine pucks	Capacity 10 samples

5. Methods

Before the biopsies can be measured at the beamline, they must be transferred into 10 µL pipette tips, the tips of which are sealed and filled with a 1% paraformaldehyde (PFA) solution.

5.1. Data acquisition

The X-ray images are taken using an X-ray microscope equipped with an LSO:Tb scintillator, which converts the monochromatic X-ray beam into visible light. In addition, an Olympus UPlanFL 20-fold objective lens and a PCO camera are used. A 10x magnification is used, resulting in a pixel size of 660 nm and a field of view of 1.32 mm x 1.32 mm. For the holotomography, four different tomograms at increasing sample-detector distances are acquired. To acquire 3D images, the sample must be rotated using the MD3 diffractometer while being exposed to the X-ray beam. Over an 181° rotation angle, 1810 projections are recorded for each distance[41]. The imaging setup at beamline P14 is shown in **Figure 12**.

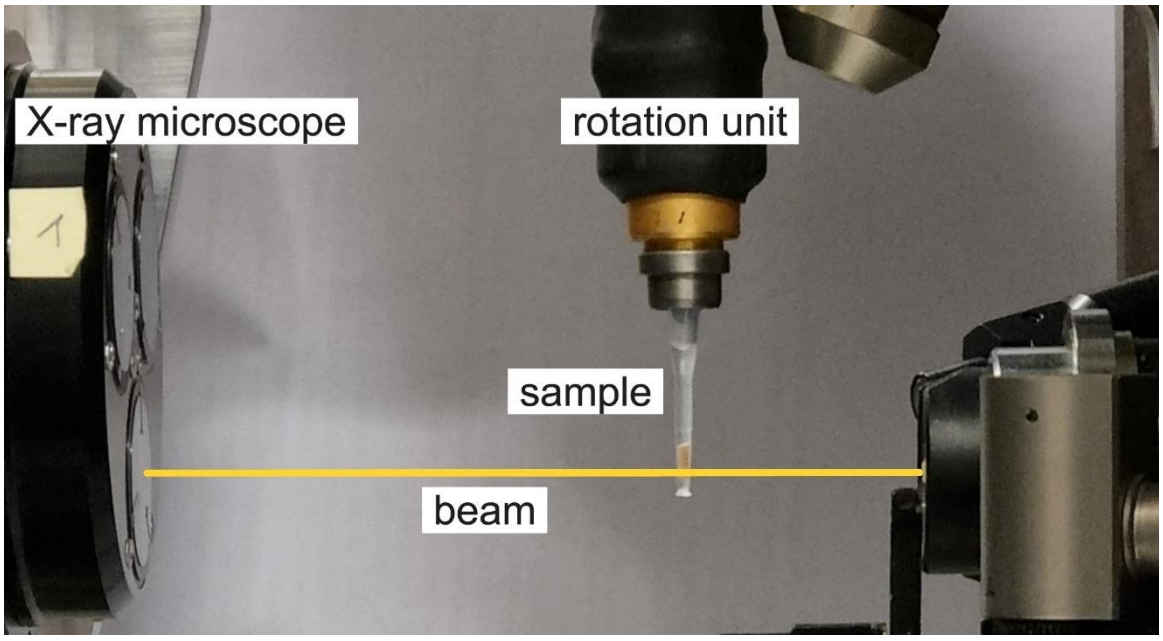

Figure 12: Typical imaging setup on EMBL beamline P14
EMBL – European Molecular Biology Laboratory

The total exposure time to the radiation for all four distances amounts to 72.4 s, resulting from a frame rate of 100 Hz and the exposure time of 10 ms per projection. An additional 100 flat-field frames are collected for each distance, which are later used for the background correction of the acquired data. In the case of kidney biopsies, a tiled acquisition is performed due to the length of the specimens. To ensure that the acquired tiles can be reassembled later, the acquired sub-scans must overlap so that they can be stitched together after the reconstruction[41].

The kidney biopsy is mounted using MARVIN and then centred using a three-click-centering approach (MXCuBE). Before data acquisition can begin, several parameters must be set, such as the energy (18 keV), the number of sub-scans with the desired offset and the four propagation distances (153 mm, 157 mm, 163 mm and 172 mm). Once the acquisition is started, all sub-scans are recorded at the first propagation distance before the detector stage is moved to the next distance. Parallel to the acquisition, the raw data is streamed to the ARAPAHO server. One of its main tasks is the correlation algorithm, which matches the received projections with the best matching flat-field frame. For more information on this task and all other tasks of the ARAPHAO server, see Albers *et al.*[41]. The 3D reconstruction pipeline, TOMO CTF, is automatically triggered after all four distances have been successfully acquired. TOMO CTF is responsible for the correction of lateral and vertical shifts due to camera movement using the flat-field frames as well as the phase retrieval, which is achieved by the multi-distance contrast-transfer function[48,49]. TOMO CTF also performs the final reconstruction of the data utilising 704 cores, resulting in a processing time of 30 s per dataset. The data acquisition steps are visualised in **Figure 13**.

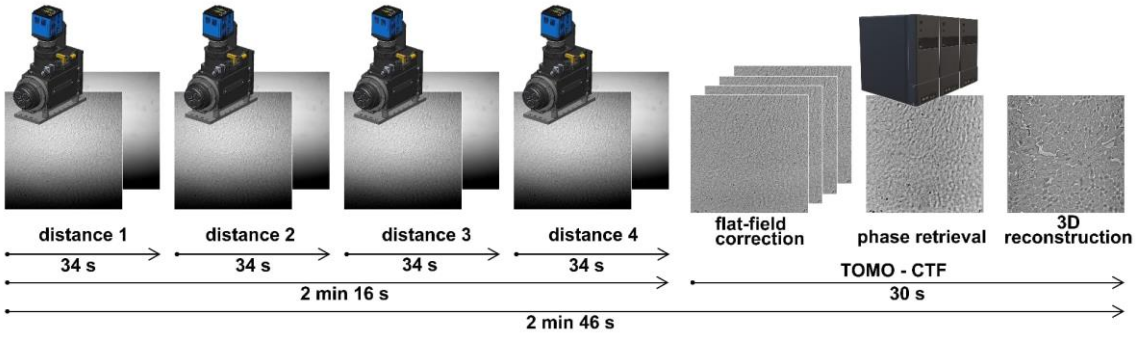

Figure 13: The processing times of the data acquisition pipeline at P14 (picture provided by Jonas Albers)

5.2. Data processing

Once the reconstructed datasets have been acquired, the data is processed so that 3D properties can be calculated and extracted. The flowchart in **Figure 14** shows the different steps that are taken.

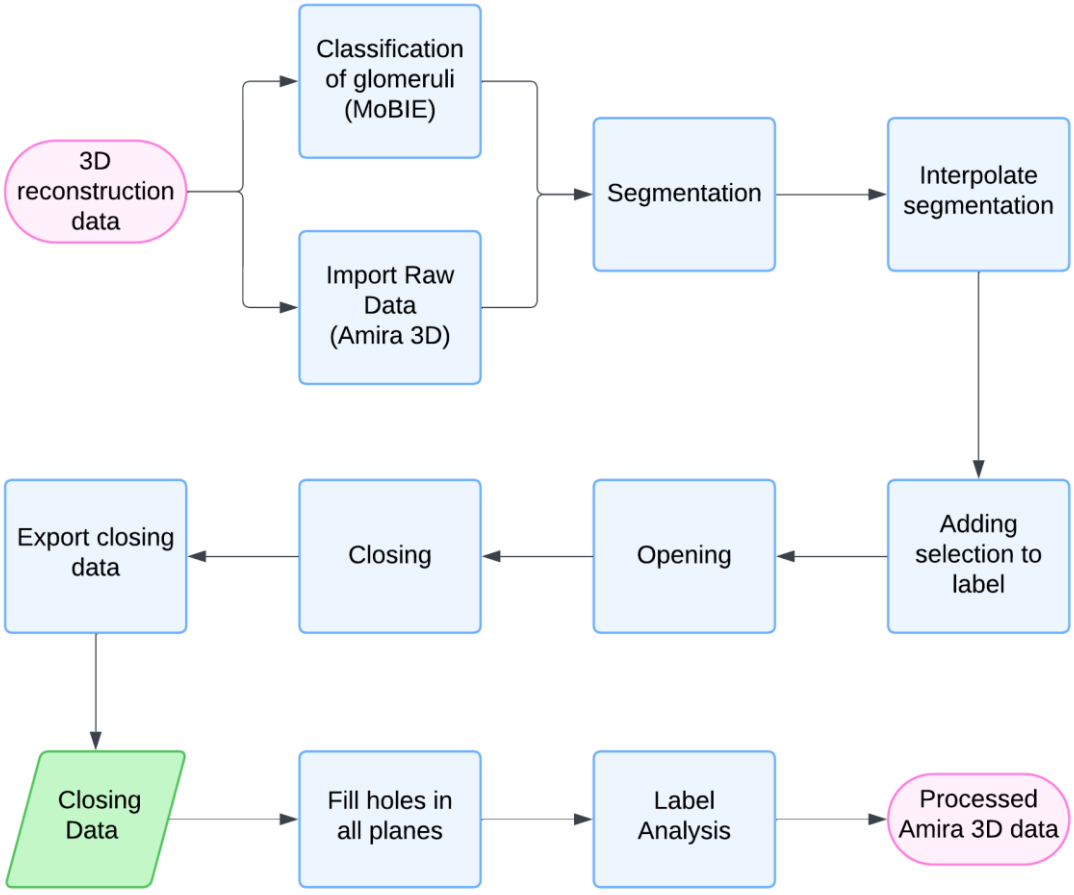

Figure 14: Flowchart of the different steps of data processing

The glomeruli located in the reconstructed datasets are identified, and their health status is classified with the help of pathologist Dr. Candice Roufosse of Imperial College London, UK. The glomeruli in each dataset are numbered according to the order in which they are identified and classified. This first step involves viewing the data on MoBIE[46].

During the classification process, glomeruli are classified into three groups: healthy, also known as open, segmentally sclerosed and globally sclerosed (**Figure 28** - **Figure 35**). **Figure 15** shows all three types of glomeruli.

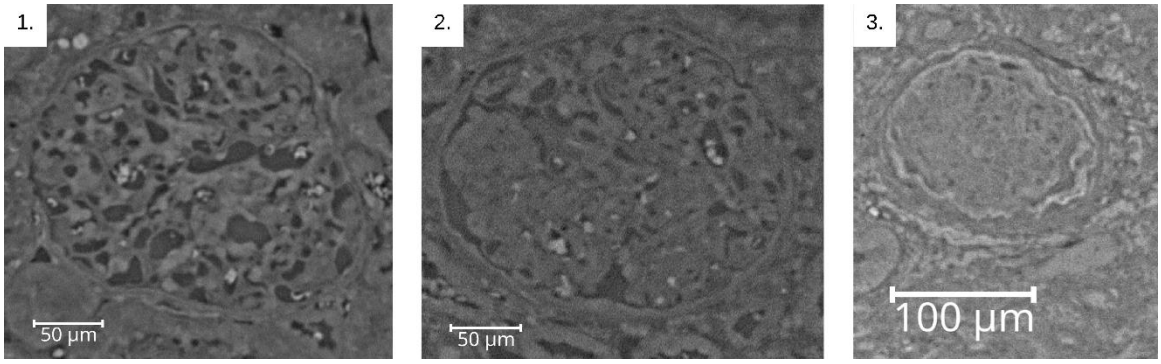

Figure 15: Comparison between an open (1.), a segmentally (2.) and a globally sclerosed (3.) glomerulus
1. Glomerulus 10 of dataset EM04639_1
2. Glomerulus 9 of dataset EM04639_1
3. Glomerulus 12 of dataset EM04633_2

The reconstructed datasets are then imported into Amira 3D, where the data can be browsed and edited. **Figure 16** shows a slice of the displayed data generated from a single dataset.

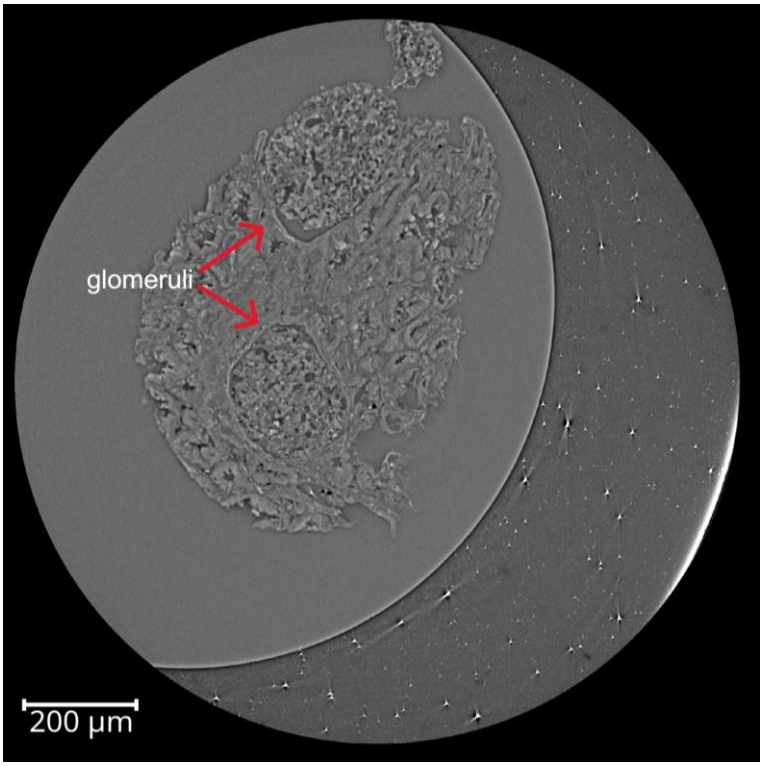

Figure 16: A cross-section of EM04596_2 in the XY plane showing two open glomeruli
Glomerulus 2 (below) and glomerulus 3 (above)

Once the data has been imported into Amira 3D, the segmentation process can begin. Segmentation must be performed manually for every glomerulus identified in each dataset. For segmentation, the previously identified glomerulus must be located in the dataset. A label is generated consisting of the glomerulus index number and the correlating health status of the glomerulus in question. After the glomerulus has been located, the next step is to outline the glomerulus and fill the outline by pressing Ctrl+F. To speed up the process, these first steps are not repeated manually for each slice of the glomerulus. Only every five to ten slices are segmented manually, as described above. The remaining slices between the segmented slices can be processed automatically by interpolating (Ctrl+I). In this process, the gaps between the manual annotations are filled. In the last step, the segmentation is added to the previously created label. A visualisation of these steps can be found in **Figure 17**.

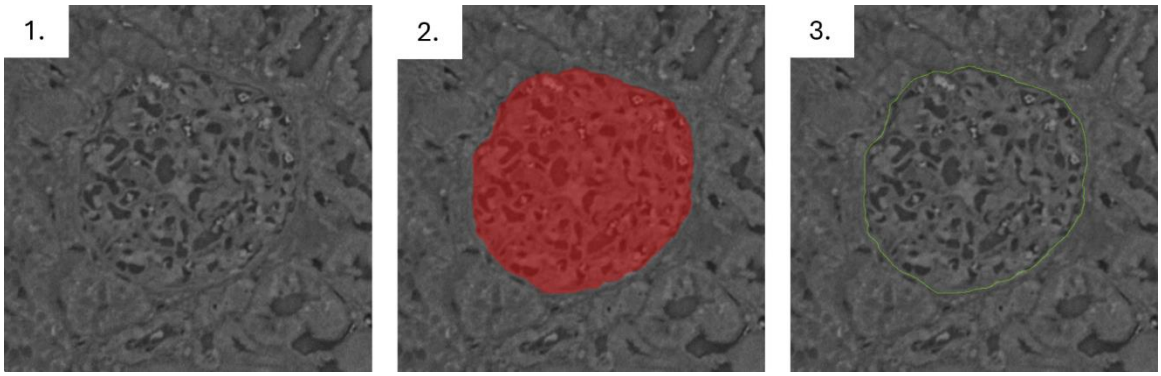

Figure 17: The three steps of the segmentation process for glomerulus 10 of EM04639_1 in the XZ plane
1. Locating the glomerulus
2. Outlining and filling the glomerulus
3. Selection added to the label 'Glom10_open'
The interpolation step is not visualised.

After all the glomeruli in a dataset have been segmented and labelled, further processing steps are performed to reduce the errors and inaccuracies introduced by manual selection and interpolation of areas in only one plane of the 3D object. The result of these inaccuracies in the XY plane can be seen in **Figure 18** (0.). Predefined processes called opening and closing are performed. These processes smooth the edges of the created object in all planes. In both processes, the type, for example, sphere, can be selected to give the program some context as to what approximate shape is expected. Furthermore, the value for the number of pixels that are smoothened can be set. Different pixel values are tested and selected, ensuring no inaccurate shapes are generated and not too much information is lost during the process.

A visualisation of the smoothing effect of opening and closing for different pixel values can be found in **Figure 18**.

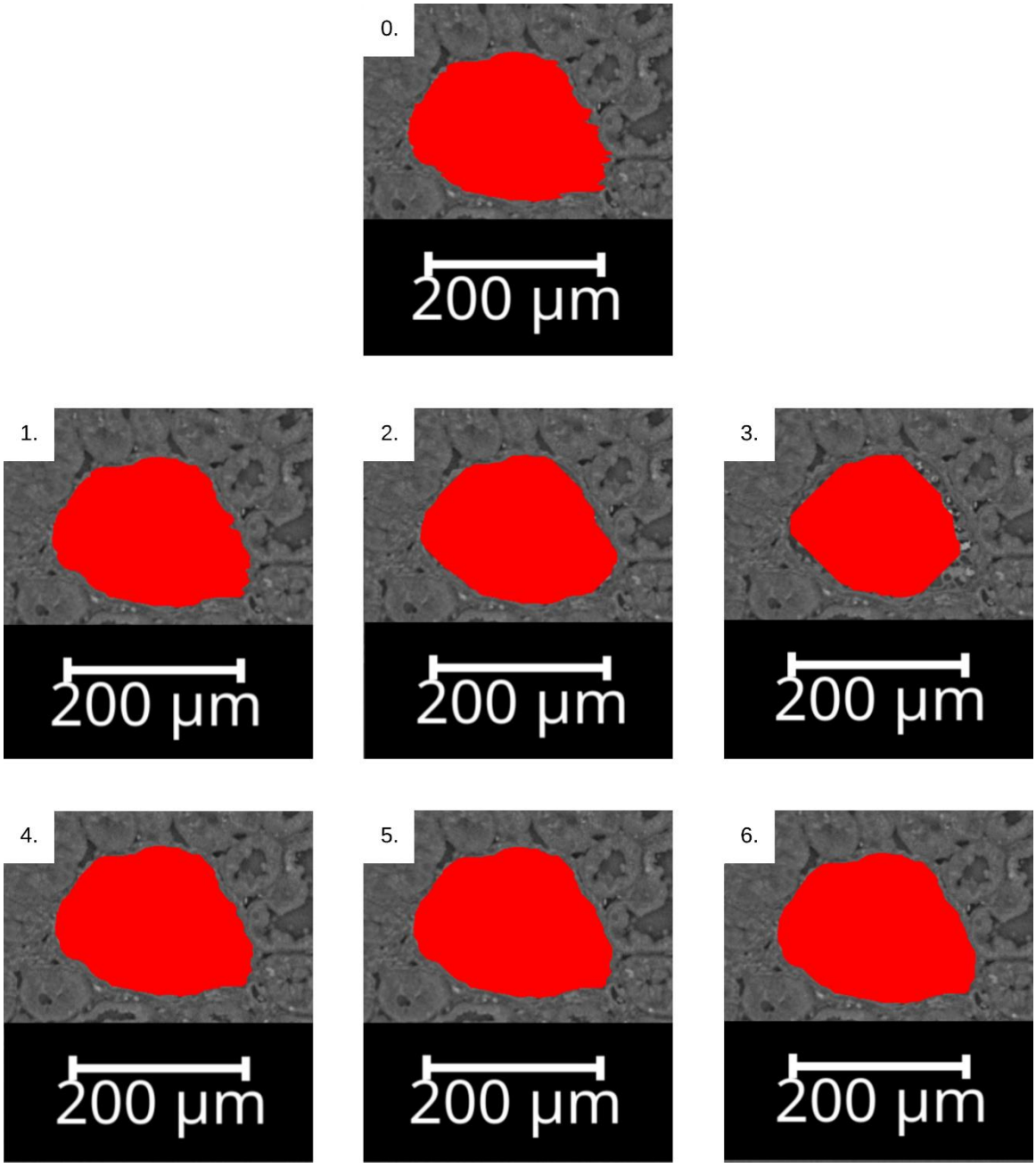

Figure 18: The effect of different opening (1.-3.) and closing (4.-6.) values for glomerulus 10 of EM04693_1 in the XY plane
0. The label of 'Glom10_open' without processing
1. – 3. 'Glom10_open' after opening with 7 (1.), 50 (2.) and 100 (3.) as the pixel smoothing value
The closing operation was performed based on opening with 7 (1.) as the pixel smoothing value
4. – 6. 'Glom10_open' after closing with 15 (4.), 50 (5.) and 100 (6.) as the pixel smoothing value

After the opening (7) and closing (15) values have been selected and the operations performed, the resulting closing data is exported. The exported data is opened in Amira 3D to perform a 'Label Analysis'. Before this analysis can be performed, all holes in all planes of each label must be filled to ensure that the calculations in the analysis are not distorted. The 'Label Analysis' delivers values for the volume, the surface area, the sphericity and the centre in all planes of all objects in a dataset, as well as a maximum, minimum and median value for all these properties across all the labels analysed. The manual segmentation process is highly time-consuming. The duration of the segmentation process and all subsequent data processing steps for a single dataset is dependent on the dimensions of the segmented glomeruli and the number of glomeruli present within the biopsy. For a typical dataset, this process can take between one to two weeks.

The statistical analyses were performed using Excel, based on the values extracted from the Amira 3D data. The statistical analyses comprised a series of t-tests to determine if the differences in the average volume and surface area between different groups of glomeruli are statistically significant. Furthermore, a χ^2-test was employed to ascertain whether there is a statistically significant correlation between the health status of a glomerulus and the AMR stage. For the t-test, the Excel function T.TEST was chosen using the parameters to conduct a two-tailed heteroscedastic analysis. The χ^2-test was performed using the function CHIQU.TEST and two contingency tables, one containing the observed values (**Table 5**) and one holding the expected values (**Table 12**).

6. Results

The acquired data is processed according to the methods described in chapter five (Methods) leading to the creation of a 3D object in Amira 3D. Based on the data of the 3D objects, a 3D image can be generated. In **Figure 19**, the processed data of a stitched biopsy (EM04596_2) and a 3D image generated based on this data are shown.

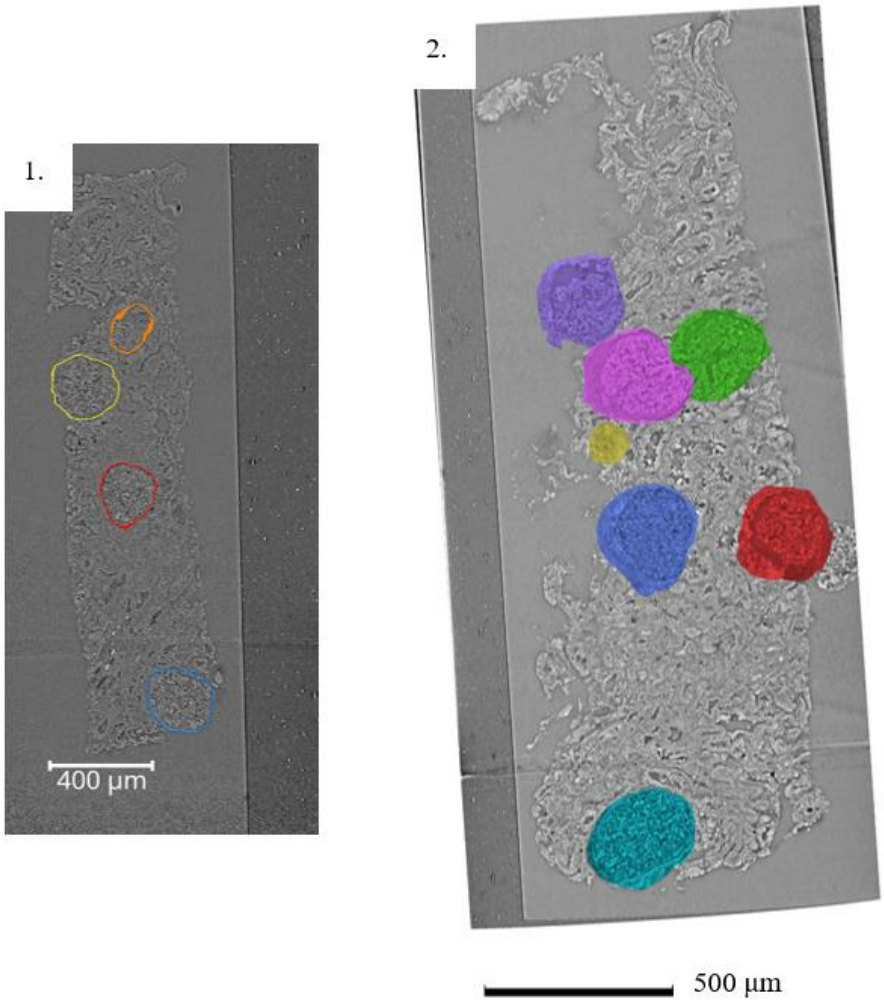

Figure 19: A cross-section of dataset EM04596_2 in the XZ plane and the generated 3D image based on the same dataset
Left: The full length of a stitched biopsy, including glomeruli 1 (blue), 3 (red), 5 (yellow) and 7 (orange)
Right: A 3D image of the same biopsy, including all seven glomeruli of the dataset (1 = light blue, 2 = red, 3 = blue, 4 = yellow, 5 = pink, 6 = green, 7 = purple)
3D – three-dimensional

In this report, 79 glomeruli were examined in relation to their health status and important properties such as volume, surface area and sphericity. Kidney tissue from six different patients was analysed. Two of the kidney biopsies (EM04596_2 & EM04691_2) showed signs of AMR in a later stage of the disease (AMR-high), while the biopsies EM04628 and EM04657_2 showed signs of an early-stage AMR (AMR-low). If there was no indication of DSA in the biopsy, these biopsies were classified as DSAneg. This was the case in EM04633_2 and EM04639_1. In the following, these labels are synonymously referred to as the type of the dataset. Most of the investigated glomeruli were classified as open and healthy, showing no signs of AMR (64%). Only 36% of the glomeruli showed signs of AMR or other damage to the tissue. A total of 22 glomeruli were classified as segmentally sclerosed (28%). The remaining 8% were classified as globally sclerosed (**Figure 20** and **Table 5**). **Figure 15** and **Figure 28** to **Figure 35** in the appendix can be used to visualise the morphology of the glomeruli in different health statuses.

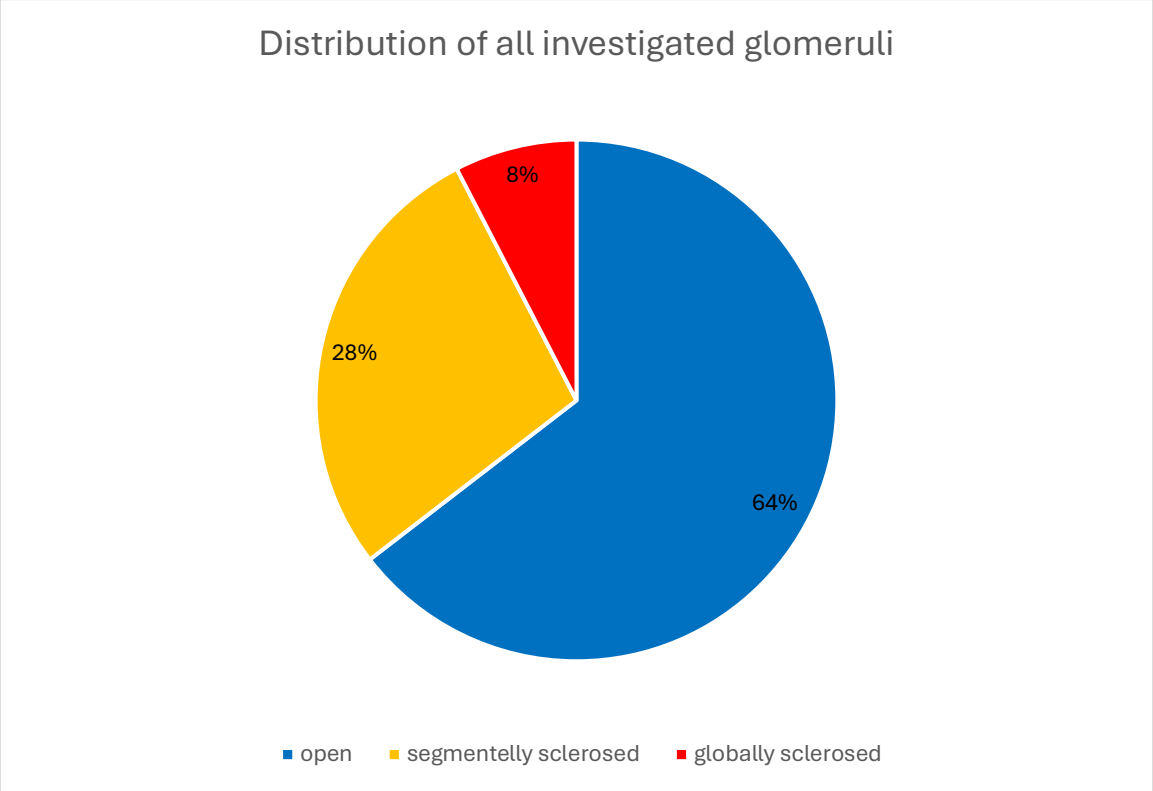

Figure 20: Distribution of the health status of all investigated glomeruli

In the following the percentages of glomeruli in a specific health state are compared to the percentages observed in all investigated glomeruli. To make representative statements about the assumed correlation between the AMR stage and the health status of the observed glomeruli. The number of investigated glomeruli correlated with their health status, and the type of dataset varied slightly due to the unpredictable number of glomeruli contained in a biopsy. In EM04596_2, only seven glomeruli were present, whereas in another biopsy (EM04657_2), 26 glomeruli were identified. In **Table 5**, the glomeruli are arranged according to their health status and the type of dataset in which they were found.

Table 5: Observed distribution of the investigated glomeruli arranged according to the different datasets and the health status of the glomeruli
AMR – antibody-mediated rejection, DSAneg – donor-specific antibodies negative

	open	**segmentally sclerosed**	**globally sclerosed**	**SUM**
AMR-high	5	8	4	17
AMR-low	29	3	1	33
DSAneg	17	11	1	29
SUM	51	22	6	79

Essential properties such as volume, surface area and sphericity provide important information about the glomeruli (**Table 11**). Taking all investigated glomeruli into account, a wide range of values can be found (**Table 6**).

Table 6: The minimum and maximum value and the median of important properties such as volume, surface area and sphericity of all glomeruli

	Volume in mm³	**Surface area in mm²**	**Sphericity**
Min	0.00046	0.03424	0.80200
Max	0.01235	0.28158	0.94800
Median	0.00451	0.14654	0.90400

This wide range of values is illustrated in **Figure 21**. Here the volume of the glomeruli and their corresponding sphericity is shown in contrast to the volume and sphericity of a perfect sphere.

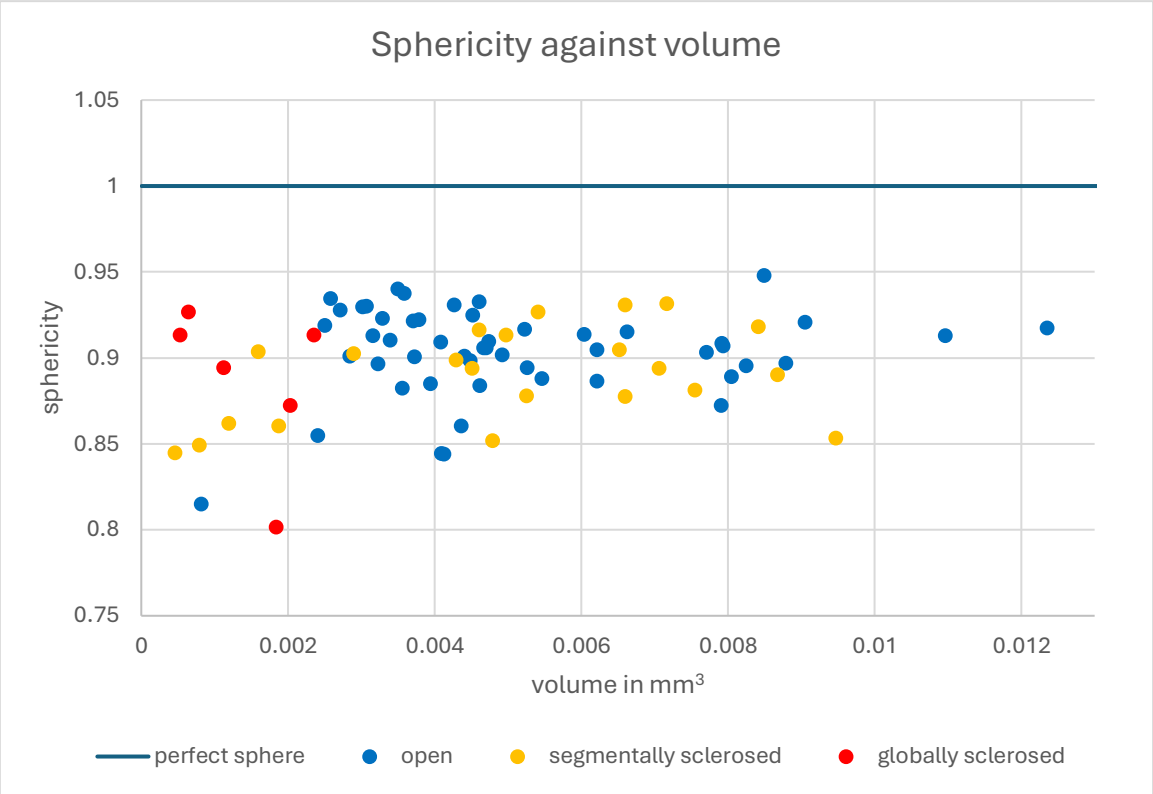

Figure 21: The volume and sphericity of all investigated glomeruli compared to a perfect sphere

While open glomeruli account for 64% of all glomeruli examined, they are underrepresented in AMR-high datasets. Here, healthy glomeruli account for only 29% of the investigated glomeruli (**Figure 22**). This equals 5 out of 17 glomeruli (**Table 5**).

In AMR-high datasets, 24% of the glomeruli were classified as globally sclerosed. About half of the investigated glomeruli show signs of AMR but are not globally sclerosed yet (**Figure 22**). The percentage of globally sclerosed glomeruli is significantly higher than the 8% they account for in all examined glomeruli (**Figure 20**).

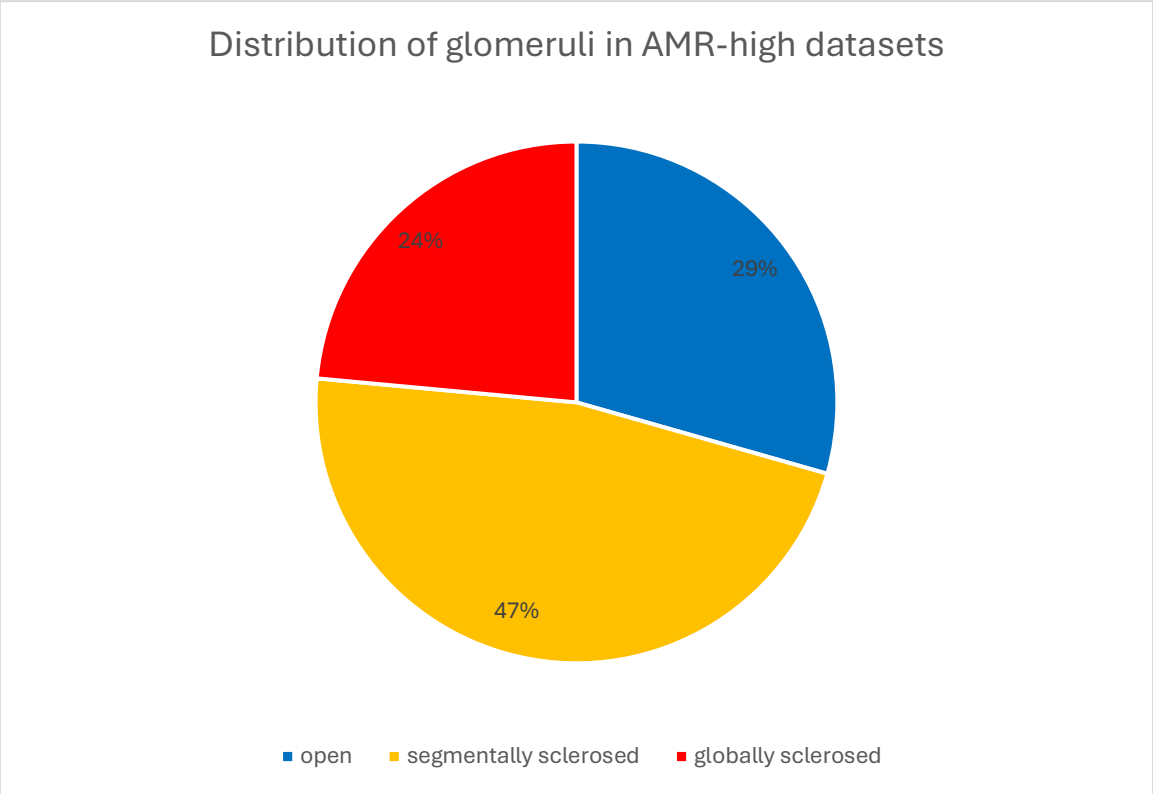

Figure 22: Distribution of the health status of the investigated glomeruli in AMR-high datasets
AMR – antibody-mediated rejection

The AMR-high datasets have the highest total number of globally sclerosed glomeruli (four). Taking all six globally sclerosed glomeruli, irrespective of the type of dataset, into account, significantly lower values for volume and surface area are observed (**Table 7**) compared to the average of all 79 glomeruli (**Table 6**).

Table 7: The minimum and maximum value and the median of important properties such as volume, surface area and sphericity of globally sclerosed glomeruli

	Volume in mm³	**Surface area in mm²**	**Sphericity**
Min	0.00053	0.03479	0.80200
Max	0.00235	0.09365	0.92700
Median	0.00148	0.07366	0.90400

The volume and the corresponding sphericity of all glomeruli present in AMR-high datasets are shown in contrast to the volume of a perfect sphere (**Figure 23**).

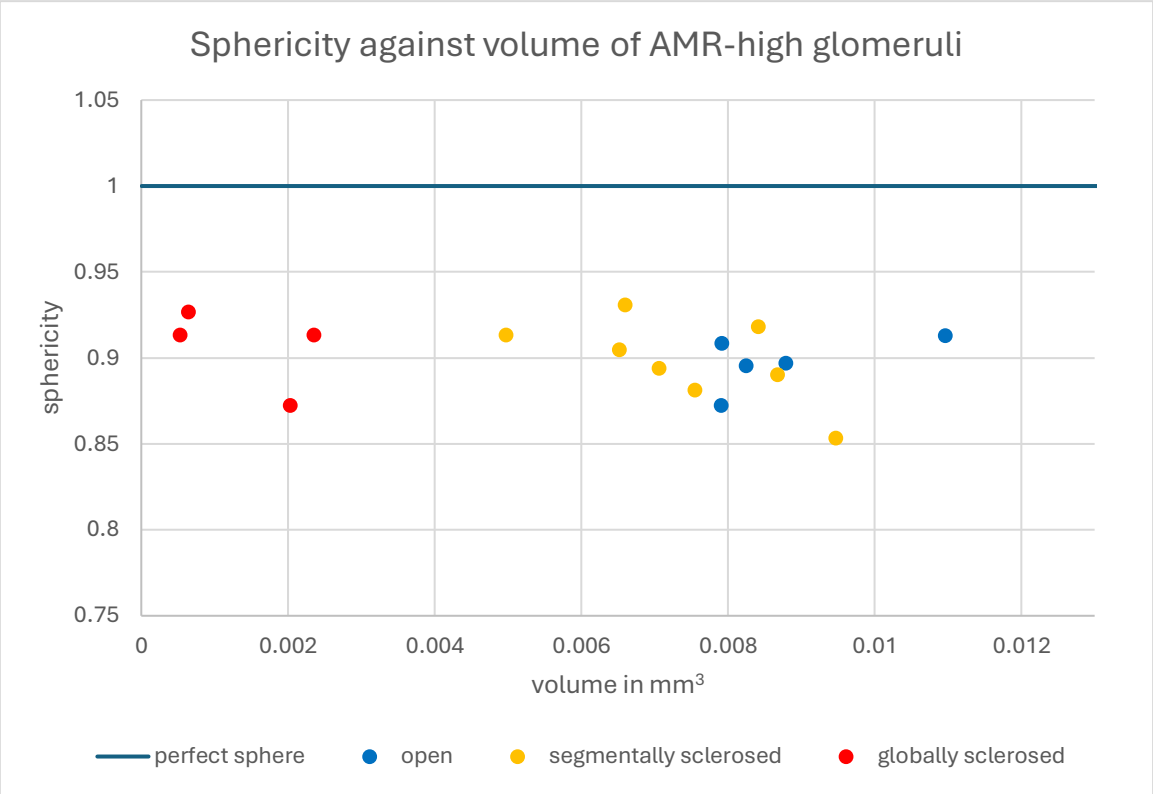

Figure 23: The volume and sphericity of all investigated glomeruli in AMR-high datasets compared to a perfect sphere
AMR – antibody-mediated rejection

In AMR-low datasets, open glomeruli are compared to all investigated glomeruli, overrepresented, while segmentally and globally sclerosed glomeruli are underrepresented. Here healthy glomeruli account for 88% of the glomeruli examined (**Figure 24**). This corresponds to 29 out of 33 glomeruli (**Table 5**). Globally sclerosed and segmentally sclerosed glomeruli represent only 12% of the examined glomeruli in AMR-low datasets. This is significantly lower than the 36% they account for in all examined glomeruli regardless of the analysed type of dataset (**Figure 20**).

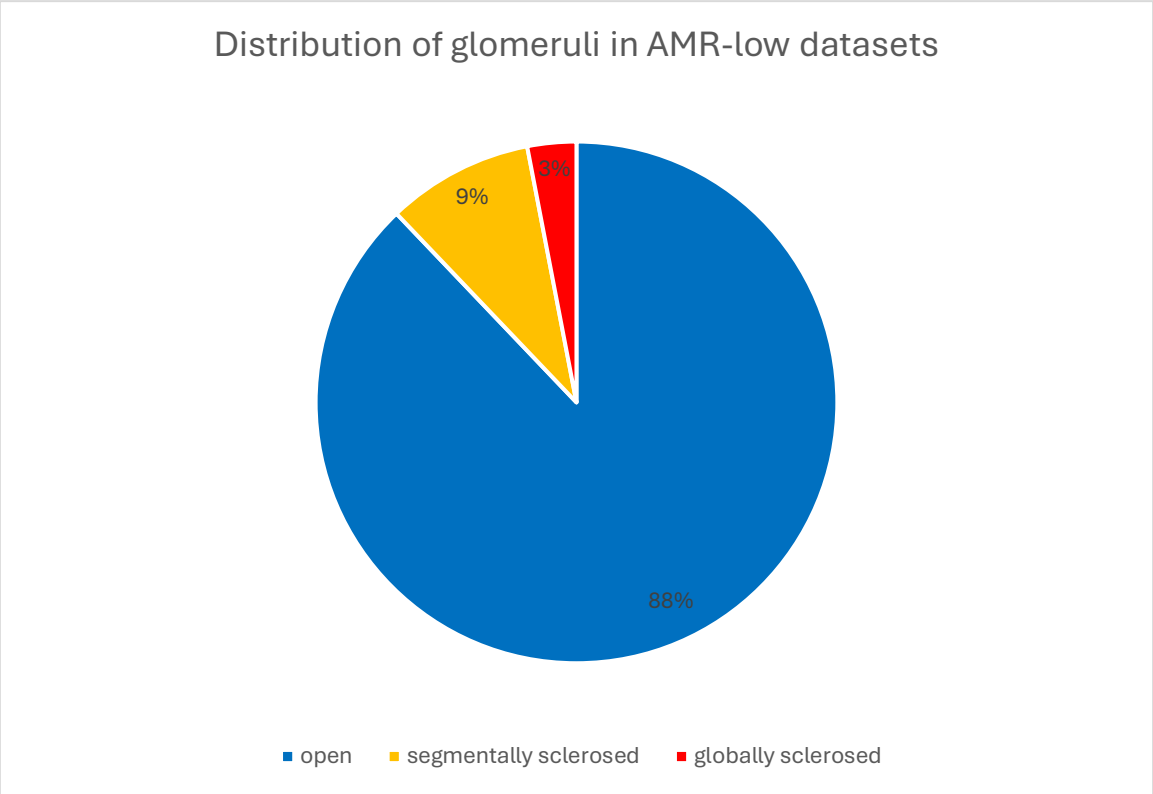

Figure 24: Distribution of the health status of the investigated glomeruli in AMR-low datasets
AMR – antibody-mediated rejection

29 of the 51 healthy glomeruli were found in AMR-low datasets (**Table 5**). Considering all 51 open glomeruli, a wide range of values for volume and surface area are observed (**Table 8**) similar to the average of all 79 glomeruli (**Table 6**).

Table 8: The minimum and maximum value and the median of important properties such as volume, surface area and sphericity of open glomeruli

	Volume in mm³	**Surface area in mm²**	**Sphericity**
Min	0.00082	0.05201	0.81500
Max	0.01235	0.28158	0.94800
Median	0.00448	0.14654	0.90700

Figure 25 shows the volume and the corresponding sphericity of all glomeruli present in AMR-low datasets, in correlation to their health status, as opposed to the volume of a perfect sphere.

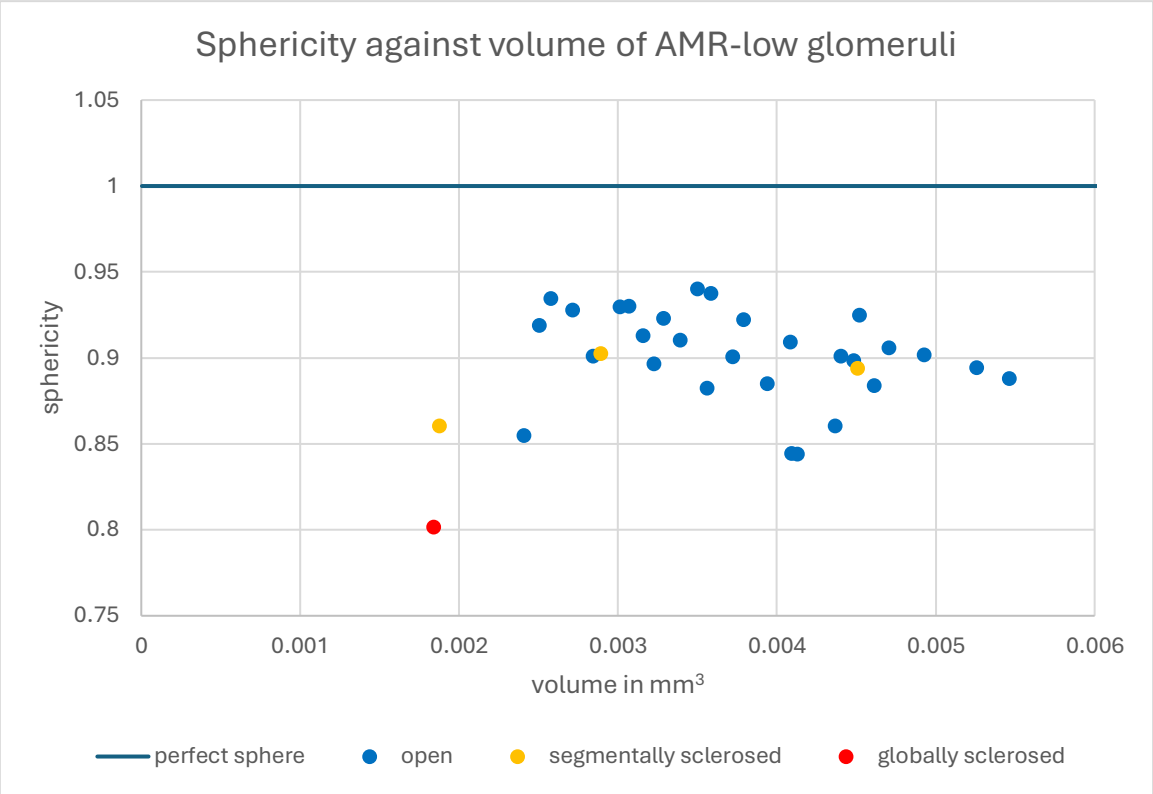

Figure 25: The volume and sphericity of all investigated glomeruli in AMR-low datasets compared to a perfect sphere
AMR – antibody-mediated rejection

Segmentally sclerosed glomeruli are overrepresented in the control datasets that showed no signs of AMR, indicating severe damage to the glomeruli. However, this damage must be attributed to diseases other than AMR. Here they account for 38% of the examined glomeruli (**Figure 26**), or 11 out of 29 glomeruli (**Table 5**). Globally sclerosed and open glomeruli account for 62% of the investigated glomeruli in DSAneg datasets, which is lower than the 72% they account for in all examined glomeruli regardless of the analysed type of dataset (**Figure 20**).

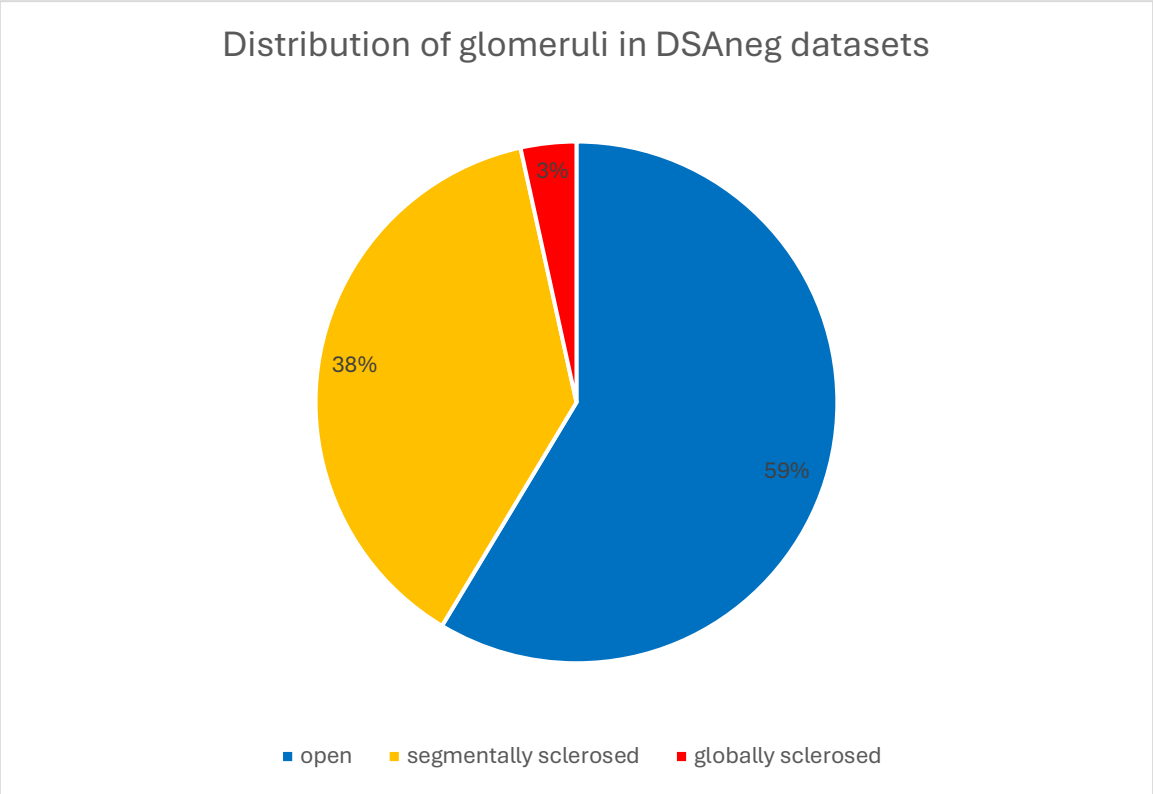

Figure 26: Distribution of the health status of the investigated glomeruli in DSAneg datasets
DSAneg – donor-specific antibody negative

50% of all segmentally sclerosed glomeruli can be found in DSAneg datasets, which equals 11 out of 22 (**Table 5**). Considering all 22 glomeruli, a wide range of values for volume and surface area can be observed, with a higher median than all examined glomeruli (**Table 9** & **Table 6**).

Table 9: The minimum and maximum value and the median of important properties such as volume, surface area and sphericity of segmentally sclerosed glomeruli

	Volume in mm³	**Surface area in mm²**	**Sphericity**
Min	0.00046	0.03424	0.84500
Max	0.00947	0.25367	0.93200
Median	0.00511	0.16108	0.89400

The volume and the corresponding sphericity of all glomeruli present in the control datasets, regardless of their health status, are shown in contrast to the volume of a perfect sphere (**Figure 27**).

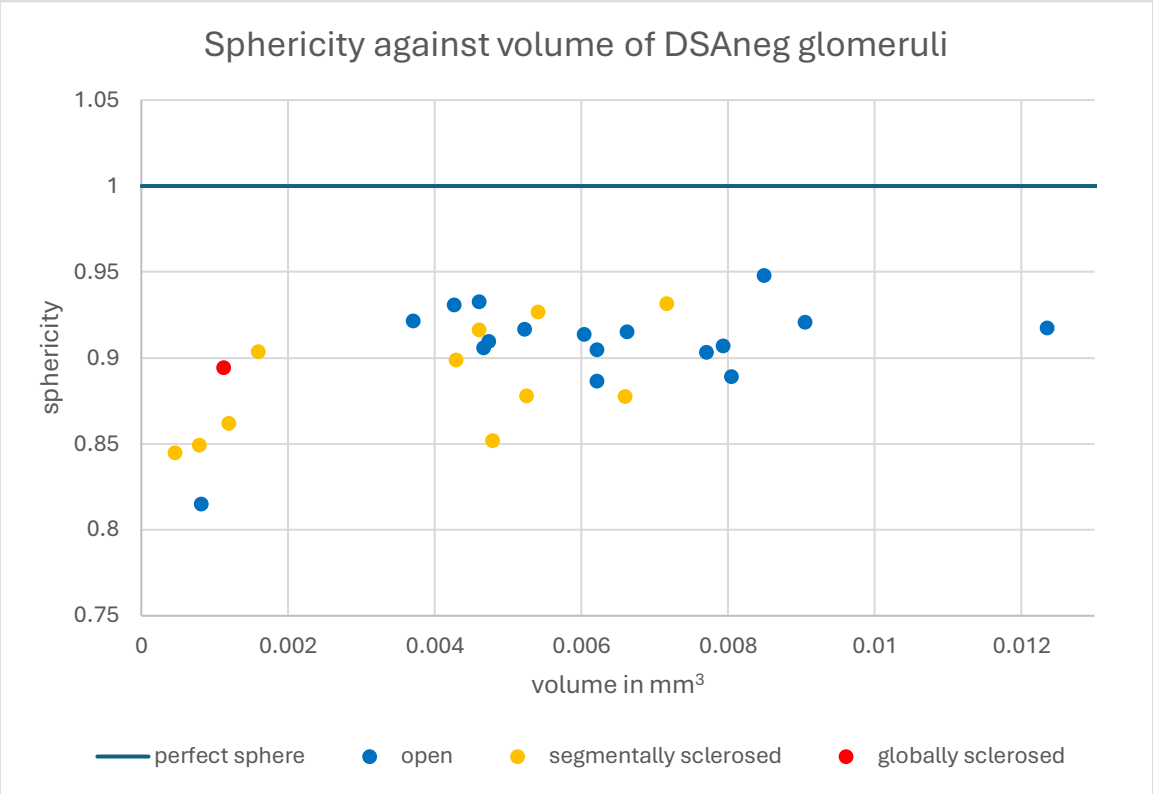

Figure 27: The volume and sphericity of all investigated glomeruli in DSAneg datasets compared to a perfect sphere
DSAneg – donor-specific antibody negative

Furthermore, statistical analyses were performed based on the data in **Table 11**. Three heteroscedastic t-tests were performed to compare glomerular volume and surface area in different health statuses. The p-values of these analyses are shown in **Table 10**.

Table 10: P-values of the conducted t-tests

Compared health statuses	p-value for compared volumes	p-value for compared surface areas
open/segmentally sclerosed	0.9220060	0.8783308
open/globally sclerosed	0.0000001	0.0000758
Segmentally sclerosed/globally sclerosed	0.0000073	0.0000725

The t-tests showed no significant differences between the average of volume and surface area of healthy glomeruli compared to segmentally sclerosed glomeruli. However, there were significant differences in the means when comparing these properties for open and segmentally sclerosed glomeruli with globally sclerosed glomeruli.

The p-values for these four comparisons are all significantly smaller than the 0.05 threshold, meaning that the differences between the averages of the different groups are significant with approximately 100% confidence.

In addition, a χ^2 test was performed to determine if there was a correlation between the health status of a glomerulus and the type of dataset examined. This test was performed based on the values found in **Table 5** and **Table 12**. The calculated p-value was 0.00033, also exceeding the 0.05 threshold. Therefore, with a confidence of nearly 100%, it can be assumed that there is a correlation between the health status and the type of dataset.

7. Discussion

In this study, 79 glomeruli were investigated, and properties such as their volume, surface area and sphericity were analysed. Focusing on the volume, large variations were observed. The volumes ranged from 0.00046 mm^3 to 0.01235 mm^3 with a median of 0.00451 mm^3 (**Table 6**). If only open glomeruli are taken into account, similar values are observed, which is highlighted by the almost identical median of 0.00448 mm^3 (**Table 8**). In the study by Johnson *et al.*, similar values were observed, ranging from 0.00604 mm^3 to 0.01032 mm^3, representing the upper half of the glomeruli examined here[50]. The median of the volumes of the investigated open glomeruli differs by less than 1% from the median of the volumes of all 79 glomeruli. This observation may be reinforced by the fact that 51 out of 79 (64%) of the investigated glomeruli were classified as open, leading these values to disproportionately influence the overall calculated median (**Table 5** and **Figure 20**). Therefore, the values for the total glomeruli examined are neglected in the following discussion. Similar average glomerular volumes compared to the aggregated volume observed in open glomeruli were found in the studies by Macleod *et al.* (0.00421 mm^3) and Wagner (0.0042 mm^3)[51,52]. In contrast, the volumes of globally sclerosed glomeruli differ significantly from the volumes observed in open glomeruli. The maximum value for the volume of a single globally sclerosed glomerulus of 0.00235 mm^3 is significantly smaller than the maximum volume of 0.01235 mm^3 observed in an open glomerulus (**Table 7** and **Table 8**). This also affects the resulting median. The mean volume of a globally sclerosed glomerulus of 0.00148 mm^3 is approximately one third of the median of a healthy glomerulus (**Table 7** and **Table 8**). The maximum value of the investigated globally sclerosed glomeruli is near the lower range found in the studies of Azevedo *et al.* (0.0028 mm^3 – 0.0068 mm^3), Keller *et al.* (0.00279 mm^3) and within the range observed by Sasaki *et al.* (0.00231 mm^3 - 0.00535 mm^3)[53–55]. Caramori *et al.* found even smaller values ranging from 0.00174 mm^3 to 0.00211 mm^3 for the glomerular volume by studying living and deceased donor kidneys[56]. The mean volume of segmentally sclerosed glomeruli is 0.00511 mm^3 (**Table 9**). Compared to the median volume of healthy glomeruli, the average volume of segmentally sclerosed glomeruli is 14% higher (**Table 8** and **Table 9**). This phenomenon could be explained by hypertrophy. Hypertrophy delineates the swelling of cells and the enlargement of tissues and organs without an increase in the number of cells[57].

In cases where the glomerular filtration area is reduced due to glomerular diseases and nephron loss, the cells of the remaining glomeruli expand to increase their surface area in an attempt to compensate for the reduced filtration area. Compensatory hypertrophy has been studied by several researchers using rat kidneys[58–61]. There are indicators that glomerular hypertrophy is pernicious in the long term, causing more damage than it is able to compensate for[58].

The surface area values observed increase with the volume. The total values range from 0.03424 mm^2 to 0.28158 mm^2 (**Table 6**). The surface area values for glomeruli, also known as the Bowman's capsule in studies, always only refer to 2D sections of a glomerulus. With that in mind, the average 3D surface area of the glomeruli can be estimated based on the glomerular area values found in different studies. The estimated surface area based on Abdi *et al.* ranges from 0.045 mm^2 to 0.128 mm^2 (2D area: 0.0112 mm^2 – 0.0320 mm^2)[62]. Fogo *et al.* (2D area: 0.0135 mm^2) and McLachlan *et al.* (2D area: 0.0144 mm^2/0.0214mm^2) documented smaller glomerular areas, resulting in 3D surface areas of 0.054 mm^2 and 0.058 mm^2/0.086 mm^2, respectively. McLachlan *et al.* differentiate between the area of the glomerular tuft and the area of the Bowman's capsule[63,64].

Irrespective of their health status, the sphericity of all glomeruli ranges between 0.802 and 0.948 (**Table 6**). There are no significant differences between healthy, segmentally and globally sclerosed glomeruli. Their average sphericity ranges from 0.894 to 0.907 (**Table 7** - **Table 9**). Most studies investigating glomeruli and their characteristics such as volume and surface area are based on the assumption of glomerular sphericity, as described by Samuel *et al.*[65]. Therefore, 3D data is superior to 2D data as no assumptions need to be made. The overall distribution of the volume of the glomeruli studied in relation to their sphericity is shown in **Figure 21**. Showing that 13 out of all 22 segmentally sclerosed glomeruli have a sphericity of under 0.9, representing over 50% of all segmentally sclerosed glomeruli and approximately 40% of all glomeruli with a sphericity under 0.9. 50% of all globally sclerosed glomeruli (three) have a sphericity of under 0.9, but they account for less than 10% of all glomeruli with a sphericity of under 0.9. 17 open glomeruli have a sphericity of under 0.9. Although they account for over 50% of all glomeruli with a sphericity below 0.9, this only makes up about 33% of all healthy glomeruli (**Table 5** and **Figure 21**).

In AMR-high datasets, segmentally and globally sclerosed glomeruli are overrepresented compared to the distribution of the glomeruli, irrespective of the type of dataset they were located in (**Figure 20** and **Figure 22**). **Figure 23** is a good visualisation of the significantly lower volumes observed in globally sclerosed glomeruli compared to open glomeruli. In contrast **Figure 20** and **Figure 24** highlight the overrepresentation of healthy glomeruli in AMR-low datasets. It is also interesting to note that the volumes found in AMR-low dataset vary only slightly between the glomeruli of different health statuses, ranging from 0.0018 mm^3 and 0.0055 mm^3 (**Figure 25**). 50% of all examined segmentally sclerosed glomeruli are located in DSAneg datasets (**Table 5**, **Figure 20** and **Figure 26**). **Figure 27** shows the range of glomerular volumes observed for all three health statuses in DSAneg datasets, ranging from 0.00046 mm^3 to 0.01235 mm^3, similar to the distribution in AMR-high datasets (**Figure 23**).

In addition, the relation between the health status and the volume, surface area, respectively, and the health status of a glomerulus and the type of dataset was investigated using statistical analyses such as t-tests and a χ^2-test. The result of the χ^2-test supports the assumption that in a dataset with high AMR, more sclerosed glomeruli can be found. The results of the t-tests show that the volume and the surface area of a glomerulus change when it becomes globally sclerosed (**Table 10**).

The further a patient is in the AMR process, the more segmentally and globally sclerosed glomeruli can be found in a biopsy. Compared to DSAneg kidney biopsies, AMR-low datasets consist of more healthy glomeruli due to the fact that DSAneg biopsies, although showing no signs of AMR, are clearly coming from diseased kidneys. Despite all the observations and statistical analyses showing a correlation between the health status of glomeruli, their characteristics and the type of dataset in which they were found, more research needs to be conducted. Here only a total of 79 glomeruli from six patients were investigated, which, in comparison to the 1,000,000 to 1,500,000 glomeruli in each adult kidney, is an irrelevantly small random sample. Other patient demographics such as age, gender, ethnicity and kidney weight should also be taken into account. The study by McNamara *et al.* showed significant differences in the glomerular volume between African Senegalese and African Americans[66]. Abdi *et al.* also showed differences in the glomerular area between black- and white-skinned donors[62].

In conclusion, this thesis identified a correlation between a patient's AMR stage and the health status of the investigated glomeruli. The statistical analysis of the volume and surface area of globally sclerosed glomeruli in comparison to healthy and segmentally sclerosed glomeruli further corroborates this connection. Although these findings are consistent with those of previous studies, the limited sample size restricts the generalisability of the results. It is imperative that this research be repeated on a larger scale, with additional factors such as patient demographics taken into consideration, in order to obtain a more reliable conclusion. This study demonstrates the potential of 3D imaging to facilitate a more comprehensive understanding of AMR's impact and enhance diagnostic strategies. The combination of different imaging techniques, such as 3D X-ray imaging and EM, would allow for a more comprehensive understanding of the impact of AMR on glomeruli. For example, the data obtained through 3D X-ray imaging could be employed to identify regions of interest within the biopsy sample, thereby enabling a targeted investigation of the region in question through the use of EM. Furthermore, this method offers the potential for training a machine learning algorithm to automate the segmentation process in the future. This would facilitate a more thorough investigation of the impact of AMR in glomeruli, making it feasible for researchers to conduct a study encompassing a wide range of groups of interest.

8. Ethics statement

Human samples used in this research project were obtained from the Imperial College Healthcare Tissue & Biobank. The Imperial College Healthcare Tissue & Biobank is supported by the National Institute for Health Research Biomedical Research Centre based at Imperial College Healthcare National Institute for Health Trust and Imperial College London. The Imperial College Healthcare Tissue & Biobank is approved by Wales REC3 to release human material for research (22/WA/2836).

EMBL Ethical approval for the project Schwab / Duke / Uhlmann - A Nanopathology Platform for Prediction and Early Detection of Disease in Kidney Transplant Rejection - (BIAC 2022-032) was granted in December 2022.

9. Acknowledgements

I would like to express my sincerest gratitude to EMBL for allowing me the opportunity to conduct my bachelor's thesis under their guidance. I am particularly grateful to the members of the Duke Team for their insightful advice and assistance, which greatly contributed to my understanding of this complex research project. I am especially indebted to Ph. D. Elizabeth Duke for her exceptional supervision, invaluable insights, and expertise, which were crucial to the successful completion of this thesis. In connection with this research project, I would also like to thank Ph. D. Matthew Lawson and Dr. Candice Roufosse for introducing me to the research project and providing histopathological insides.

Furthermore, I would like to express my gratitude to Prof. Dr. Jörg Andrä for his supervision, a listening ear and for giving me the courage to switch companies. This ultimately led to the opportunity to work at EMBL which I am immensely grateful for.

Finally, I would like to acknowledge the support of my family, friends and partner Michael. Each and every one of you provided me with the needed strength, perseverance and self-esteem to successfully finish my thesis.

Last but not least, I would like to thank my father for always believing in me and my dreams, even if he cannot be at my side to witness their fruition. I miss you every day, but I know I am not alone in this sentiment. It is comforting to know you are never truly gone because you will always be in my heart.

10. Affidavit

I, Anna Kischlat, hereby confirm that the present bachelor´s thesis was independently written by me without any external or unauthorised aids.

All sources which have been used to finish this work are indicated as such.

Furthermore, I confirm that this thesis has not been submitted as part of another examination process nor in identical form.

Hamburg, the 3rd of December 2024

Anna Kischlat

11. References

1. Benefits and risks of a kidney transplant. *Organ transplantation - NHS Blood and Transplant* https://www.nhsbt.nhs.uk/organ-transplantation/kidney/benefits-and-risks-of-a-kidney-transplant/ - accessed: 01.11.2024.
2. Number of kidney transplants worldwide by region 2022 | Statista. https://www.statista.com/statistics/398657/kidney-transplants-by-world-region/ - accessed: 01.11.2024.
3. Kim, M., Martin, S. T., Townsend, K. R. & Gabardi, S. Antibody-Mediated Rejection in Kidney Transplantation: A Review of Pathophysiology, Diagnosis, and Treatment Options. *Pharmacother. J. Hum. Pharmacol. Drug Ther.* **34**, 733–744 (2014).
4. Loupy, A. *et al.* The Banff 2019 Kidney Meeting Report (I): Updates on and clarification of criteria for T cell– and antibody-mediated rejection. *Am. J. Transplant.* **20**, 2318 (2020).
5. Baldwin, W. M., Valujskikh, A. & Fairchild, R. L. Mechanisms of antibody-mediated acute and chronic rejection of kidney allografts. *Curr. Opin. Organ Transplant.* **21**, 7–14 (2016).
6. Park, B. H., Kim, Y. N. & Shin, H. S. New treatment for antibody-mediated rejection: interleukin-6 inhibitors. *Clin. Transplant. Res.* **38**, 1–6 (2024).
7. Wood, K. J. & Goto, R. Mechanisms of Rejection: Current Perspectives. *Transplantation* **93**, 1–10 (2012).
8. Montgomery, R. A., Loupy, A. & Segev, D. L. Antibody-mediated rejection: New approaches in prevention and management. *Am. J. Transplant.* **18**, 3–17 (2018).
9. Racusen, L. C. & Haas, M. Antibody-Mediated Rejection in Renal Allografts: Lessons from Pathology. *Clin. J. Am. Soc. Nephrol.* **1**, 415–420 (2006).

10. Botermans, J. M. *et al.* C4d Staining In Renal Allograft Biopsies with Early Acute Rejection and Subsequent Clinical Outcome. *Clin. J. Am. Soc. Nephrol. CJASN* **6**, 1207 (2011).
11. Deng, F., Miller, J. & Swanson, T. Histology Revolution: from inefficient, two-dimensional, and low-resolution techniques to high-throughput, three-dimensional and high-resolution techniques. *Egypt. J. Histol.* **0**, 0–0 (2019).
12. Murray, I. V. & Paolini, M. A. Histology, Kidney and Glomerulus. in *StatPearls* (StatPearls Publishing, Treasure Island (FL), 2024).
13. Boron, W. F. & Boulpaep, E. L. *Medical Physiology: A Cellular and Molecular Approach*. (Elsevier Saunders, Philadelphia, Pa, 2005).
14. Nephron | Definition, Function, Structure, Diagram, & Facts | Britannica. https://www.britannica.com/science/nephron - accessed: 13.11.2024.
15. Kardasz, S. The function of the nephron and the formation of urine. *Anaesth. Intensive Care Med.* **13**, 309–314 (2012).
16. *Immunobiology 5: The Immune System in Health and Disease*. (Garland Pub, New York, 2001).
17. Roufosse, C. How to implement Banff Lesions Scores as new endpoints in clinical trials. (2023).
18. Gurina, T. S. & Simms, L. Histology, Staining. in *StatPearls* (StatPearls Publishing, Treasure Island (FL), 2024).
19. Butte, A. J. & Chen, D. Translational Bioinformatics for Genomic Medicine. in *Genomic and Personalized Medicine* 272–286 (Elsevier, 2013). doi:10.1016/B978-0-12-382227-7.00023-9.
20. Feldman, A. T. & Wolfe, D. Tissue Processing and Hematoxylin and Eosin Staining. in *Histopathology* (ed. Day, C. E.) vol. 1180 31–43 (Springer New York, New York, NY, 2014).

21. IHC vs IF: A Thorough Comparison for Research. https://www.histologix.com/insights-news/ihc-vs-if-a-thorough-comparison-for-research/ (2023) - accessed: 16.11.2024.
22. Lees, G. E., Cianciolo, R. E. & Clubb, F. J. Renal Biopsy and Pathologic Evaluation of Glomerular Disease. *Top. Companion Anim. Med.* **26**, 143–153 (2011).
23. Akgul, M. & Williamson, S. R. Immunohistochemistry for the diagnosis of renal epithelial neoplasms. *Semin. Diagn. Pathol.* **39**, 1–16 (2022).
24. Nasr, S. H., Fidler, M. E. & Said, S. M. Paraffin Immunofluorescence: A Valuable Ancillary Technique in Renal Pathology. *Kidney Int. Rep.* **3**, 1260–1266 (2018).
25. Wittekind, D. Traditional staining for routine diagnostic pathology including the role of tannic acid. 1. Value and limitations of the hematoxylin-eosin stain. *Biotech. Histochem.* **78**, 261–270 (2003).
26. Jensen, E. Types of Imaging, Part 1: Electron Microscopy. *Anat. Rec.* **295**, 716–721 (2012).
27. Sarret, G. *et al.* Use of Synchrotron-Based Techniques to Elucidate Metal Uptake and Metabolism in Plants. in *Advances in Agronomy* vol. 119 1–82 (Elsevier, 2013).
28. Conti, S. *et al.* Early and late scanning electron microscopy findings in diabetic kidney disease. *Sci. Rep.* **8**, 4909 (2018).
29. Forschung - Universität Regensburg. https://www.uni-regensburg.de/biologie-vorklinische-medizin/molekulare-zellulaere-anatomie/forschung/index.html - accessed: 30.11.2024.
30. Inkson, B. J. 2 - Scanning electron microscopy (SEM) and transmission electron microscopy (TEM) for materials characterization. *Scan. Electron Microsc.*
31. Panchbhai, A. Wilhelm Conrad Röntgen and the discovery of X-rays: Revisited after centennial. *J. Indian Acad. Oral Med. Radiol.* **27**, 90 (2015).
32. Jensen, M. & Wilhjelm, J. E. X-ray imaging: Fundamentals and planar imaging.

33. Tafti, D. & Maani, C. V. X-ray Production. in *StatPearls* (StatPearls Publishing, Treasure Island (FL), 2024).
34. Heaton, B. & Dendy, P. P. *Physics for Diagnostic Radiology, Third Edition*.
35. Jensen, M. & Wilhjelm, J. E. CT scanning.
36. X-Rays. *National Institute of Biomedical Imaging and Bioengineering* https://www.nibib.nih.gov/science-education/science-topics/x-rays - accessed: 03.11.2024.
37. How does a synchrotron radiation source work? https://photon-science.desy.de/research/students__teaching/primers/synchrotron_radiation/index_eng.html - accessed: 05.11.2024.
38. Leserexkursion am 19. April 2024: Besuchen Sie mit Spektrum das DESY in Hamburg. https://www.spektrum.de/alias/leserexkursion-am-19-april-2024/besuchen-sie-mit-spektrum-das-desy-in-hamburg/2204190 - accessed: 05.11.2024.
39. Storage Rings as Synchrotron Radiation Sources. https://photon-science.desy.de/research/students__teaching/primers/storage_rings__beamlines/index_eng.html - accessed: 05.11.2024.
40. Machine Parameters PETRA III (Design Values). https://photon-science.desy.de/facilities/petra_iii/machine/parameters/index_eng.html - accessed: 05.11.2024.
41. Albers, J. *et al.* High Throughput Tomography (HiTT) on EMBL beamline P14 on PETRA III. *J. Synchrotron Radiat.* **31**, 186–194 (2024).
42. Gureyev, T. E. *et al.* Refracting Röntgen's rays: Propagation-based x-ray phase contrast for biomedical imaging. *J. Appl. Phys.* **105**, 102005 (2009).
43. Phase-contrast imaging. *Excillum* https://www.excillum.com/x-ray-methods/x-ray-imaging/phase-contrast-imaging/ - accessed: 13.11.2024.

44. Diemoz, P. C., Bravin, A. & Coan, P. Theoretical comparison of three X-ray phase-contrast imaging techniques: propagation-based imaging, analyzer-based imaging and grating interferometry. *Opt. Express* **20**, 2789 (2012).
45. Albers, J., Svetlove, A. & Duke, E. Synchrotron X-ray imaging of soft biological tissues – principles, applications and future prospects. *J. Cell Sci.* **137**, jcs261953 (2024).
46. Pape, C. *et al.* MoBIE: a Fiji plugin for sharing and exploration of multi-modal cloud-hosted big image data. *Nat. Methods* **20**, 475–476 (2023).
47. Gürsoy, D., De Carlo, F., Xiao, X. & Jacobsen, C. TomoPy: a framework for the analysis of synchrotron tomographic data. *J. Synchrotron Radiat.* **21**, 1188–1193 (2014).
48. Cloetens, P. *et al.* Holotomography: Quantitative phase tomography with micrometer resolution using hard synchrotron radiation x rays. *Appl. Phys. Lett.* **75**, 2912–2914 (1999).
49. Zabler, S., Cloetens, P., Guigay, J.-P., Baruchel, J. & Schlenker, M. Optimization of phase contrast imaging using hard x rays. *Rev. Sci. Instrum.* **76**, 073705 (2005).
50. Johnson, K. J., Wreford, N. G., Hoy, W. E. & Bertram, J. F. Estimating total glomerular number in human kidneys with a physical disector/fractionator combination. *Image Anal. Stereol.* **19**, 105 (2011).
51. Macleod, J. M., White, K. E., Tate, H. & Bilous, R. W. Measurement of glomerular volume in needle biopsy specimens. *Nephrol. Dial. Transplant.* **15**, 239–243 (2000).
52. Wagner, J. G. Influence of Formulation on Therapeutic Activity 2. Excretion and Metabolism of Drugs, Nomenclature and Symbolism, Fundamental Principles and Concepts. *Drug Intell.* **2**, 80–85 (1968).
53. Azevedo, F. *et al.* Glomerular Size in Early Protocol Biopsies is Associated with Graft Outcome. *Am. J. Transplant.* **5**, 2877–2882 (2005).

54. Keller, G., Zimmer, G., Mall, G., Ritz, E. & Amann, K. Nephron Number in Patients with Primary Hypertension. *N. Engl. J. Med.* **348**, 101–108 (2003).

55. Sasaki, T. *et al.* Bowman Capsule Volume and Related Factors in Adults With Normal Renal Function. *Kidney Int. Rep.* **3**, 314–320 (2018).

56. Caramori, M. L., Basgen, J. M. & Mauer, M. Glomerular Structure in the Normal Human Kidney: Differences between Living and Cadaver Donors. *J. Am. Soc. Nephrol.* **14**, 1901–1903 (2003).

57. Goss, R. J. Hypertrophy versus Hyperplasia: How much organs can grow depends on whether their functional units increase in size or in number. *Science* **153**, 1615–1620 (1966).

58. Brenner, B. M. Nephron adaptation to renal injury or ablation. *Am. J. Physiol.-Ren. Physiol.* **249**, F324–F337 (1985).

59. Hayslett, J. P., Kashgarian, M. & Epstein, F. H. Functional Correlates of Compensatory Renal Hypertrophy.

60. Olivetti, G., Anversa, P., Rigamonti, W., Vitali-Mazza, L. & Loud, A. V. Morphometry of the renal corpuscle during normal postnatal growth and compensatory hypertrophy. A light microscope study. *J. Cell Biol.* **75**, 573–585 (1977).

61. Seyer-Hansen, K., Gundersen, H. J. G. & Østerby, R. Stereology of the rat kidney during compensatory renal hypertrophy. *Acta Pathol. Microbiol. Scand. Ser. Pathol.* **93A**, 9–12 (1985).

62. Abdi, R., Slakey, D., Kittur, D. & Racusen, L. Heterogeneity of glomerular size in normal donor kidneys: Impact of race. *Am. J. Kidney Dis.* **32**, 43–46 (1998).

63. Fogo, A. *et al.* Glomerular hypertrophy in minimal change disease predicts subsequent progression to focal glomerular sclerosis. *Kidney Int.* **38**, 115–123 (1990).

64. McLachlan, M. S. F., Guthrie, J. C., Anderson, C. K. & Fulker, M. J. Vascular and glomerular changes in the ageing kidney. *J. Pathol.* **121**, 65–78 (1977).

65. Samuel, T., Hoy, W. E., Douglas-Denton, R., Hughson, M. D. & Bertram, J. F. Applicability of the glomerular size distribution coefficient in assessing human glomerular volume: the Weibel and Gomez method revisited. *J. Anat.* **210**, 578–582 (2007).

66. McNamara, B. J. *et al.* A comparison of nephron number, glomerular volume and kidney weight in Senegalese Africans and African Americans. *Nephrol. Dial. Transplant.* **25**, 1514–1520 (2010).

12. Appendix

Table 11: Overview of the collected data of all 79 glomeruli
AMR-high datasets are coloured red, AMR-low datasets green, and DSAneg datasets blue.
AMR – antibody-mediated rejection, DSAneg – donor-specific antibody negative

Dataset	Index	Volume in mm^3	Surface area in mm^2	Sphericity	Health status
EM04596_2	1	0.01096	0.26133	0.91304	open
	2	0.00825	0.22039	0.89575	open
	3	0.00791	0.21131	0.90879	open
	4	0.00065	0.03898	0.92698	globally sclerosed
	5	0.00879	0.22952	0.89723	open
	6	0.00947	0.25367	0.85346	segmentally sclerosed
	7	0.00791	0.21998	0.87252	open
EM04628	1	0.00409	0.14654	0.84460	open
	2	0.00356	0.12780	0.88256	open
	3	0.00184	0.09052	0.80174	globally sclerosed
	4	0.00241	0.10160	0.85493	open
	5	0.00526	0.16350	0.89434	open
	6	0.00547	0.16897	0.88797	open
	7	0.00188	0.08543	0.86077	segmentally sclerosed
EM04633_2	1	0.00120	0.06317	0.86217	segmentally sclerosed
	2	0.00079	0.04861	0.84953	segmentally sclerosed
	3	0.00159	0.07297	0.90395	segmentally sclerosed
	4	0.00082	0.05201	0.81498	open
	5	0.00660	0.19382	0.87765	segmentally sclerosed
	6	0.00525	0.16638	0.87794	segmentally sclerosed
	7	0.00461	0.14610	0.91663	segmentally sclerosed
	8	0.00479	0.16141	0.85187	segmentally sclerosed
	9	0.00046	0.03423	0.84495	segmentally sclerosed
	10	0.00429	0.14202	0.89885	segmentally sclerosed
	11	0.00621	0.18434	0.88651	open
	12	0.00112	0.05839	0.89434	globally sclerosed
EM04639_1	1	0.00371	0.12574	0.92163	open
	2	0.00621	0.18060	0.90508	open
	3	0.00662	0.18625	0.91550	open
	4	0.00905	0.22797	0.92104	open
	5	0.00467	0.14918	0.90586	open
	6	0.00474	0.15003	0.90973	open
	7	0.00771	0.20894	0.90328	open
	8	0.00805	0.21845	0.88911	open
	9	0.00716	0.19288	0.93171	segmentally sclerosed
	10	0.00604	0.17555	0.91400	open
	11	0.01235	0.28158	0.91776	open
	12	0.00541	0.16075	0.92676	segmentally sclerosed
	13	0.00850	0.21238	0.94806	open

Dataset	Index	Volume in mm^3	Surface area in mm^2	Sphericity	Health status
EM04639_1	14	0.00523	0.15897	0.91667	open
	15	0.00427	0.13669	0.93095	open
	16	0.00793	0.21207	0.90715	open
	17	0.00460	0.14346	0.93294	open
EM04657_2	1	0.00471	0.14990	0.90602	open
	2	0.00359	0.12084	0.93770	open
	3	0.00250	0.09703	0.91894	open
	4	0.00448	0.14635	0.89855	open
	5	0.00379	0.12743	0.92254	open
	6	0.00394	0.13635	0.88499	open
	7	0.00437	0.15012	0.86062	open
	8	0.00440	0.14414	0.90118	open
	9	0.00493	0.15525	0.90177	open
	10	0.00413	0.14740	0.84434	open
	11	0.00289	0.10877	0.90264	segmentally sclerosed
	12	0.00271	0.10141	0.92783	open
	13	0.00451	0.14758	0.89420	segmentally sclerosed
	14	0.00258	0.09733	0.93462	open
	15	0.00302	0.10854	0.92977	open
	16	0.00329	0.11579	0.92333	open
	17	0.00372	0.12900	0.90073	open
	18	0.00452	0.14291	0.92485	open
	19	0.00284	0.10773	0.90101	open
	20	0.00307	0.10981	0.93016	open
	21	0.00323	0.11775	0.89656	open
	22	0.00461	0.15162	0.88400	open
	23	0.00408	0.13587	0.90925	open
	24	0.00339	0.11990	0.91050	open
	25	0.00316	0.11396	0.91311	open
	26	0.00350	0.11857	0.94018	open
EM04691_2	1	0.00652	0.18650	0.90483	segmentally sclerosed
	2	0.00053	0.03479	0.91355	globally sclerosed
	3	0.00841	0.21780	0.91843	segmentally sclerosed
	4	0.00868	0.22933	0.89056	segmentally sclerosed
	5	0.00706	0.19906	0.89422	segmentally sclerosed
	6	0.00755	0.21122	0.88131	segmentally sclerosed
	7	0.00500	0.15420	0.91341	segmentally sclerosed
	8	0.00660	0.18276	0.93082	segmentally sclerosed
	9	0.00235	0.09365	0.91331	globally sclerosed
	10	0.00203	0.08893	0.87240	globally sclerosed

Table 12: Expected distribution of the investigated glomeruli arranged according to the different datasets and the health status of the glomeruli
AMR – antibody-mediated rejection, DSAneg – donor-specific antibody negative

	open	**segmentally sclerosed**	**globally sclerosed**	**SUM**
AMR-high	10.98	4.73	1.29	17
AMR-low	21.30	9.19	2.51	33
DSAneg	18.72	8.08	2.20	29
SUM	51	22	6	79

To visualise how the values in **Table 12** were calculated an example of the calculation of the result for the category combination of open and AMR-high is given:

$$\frac{17 \cdot 51}{79} = 10.98$$

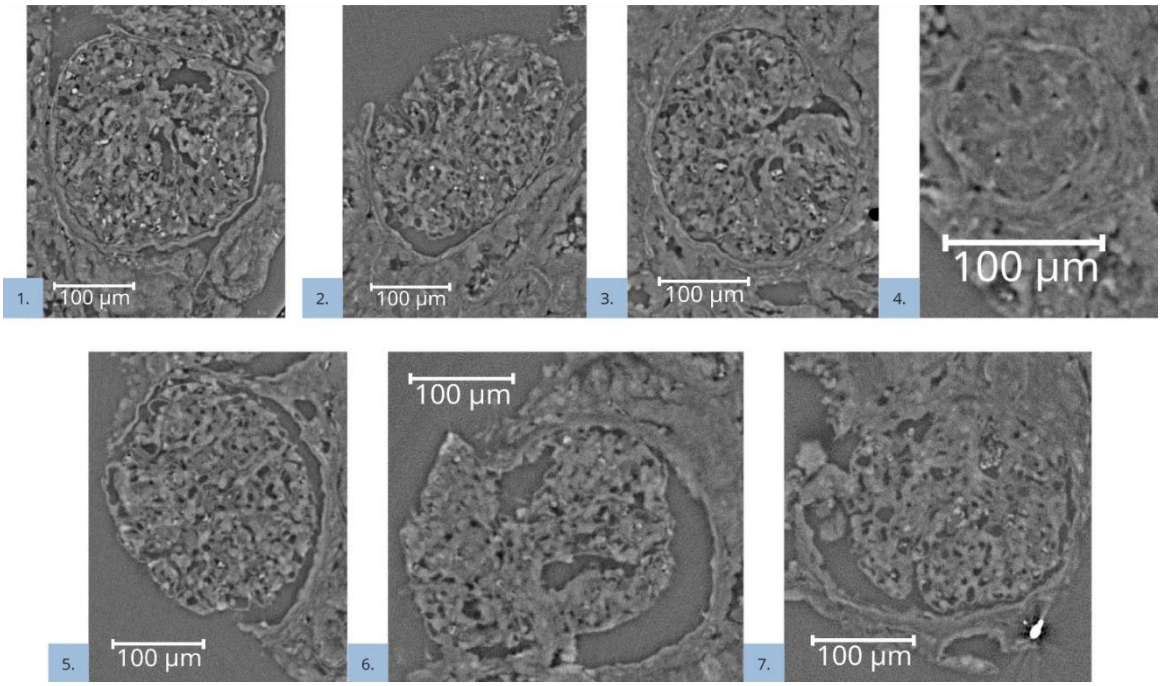

Figure 28: A cross-section of all glomeruli from AMR-high dataset EM04596_2 in the XY plane numbered according to their index
Glomeruli 1, 2, 3, 5 and 7 are open. Glomerulus 4 is globally and glomerulus 6 is segmentally sclerosed.
AMR – antibody-mediated rejection

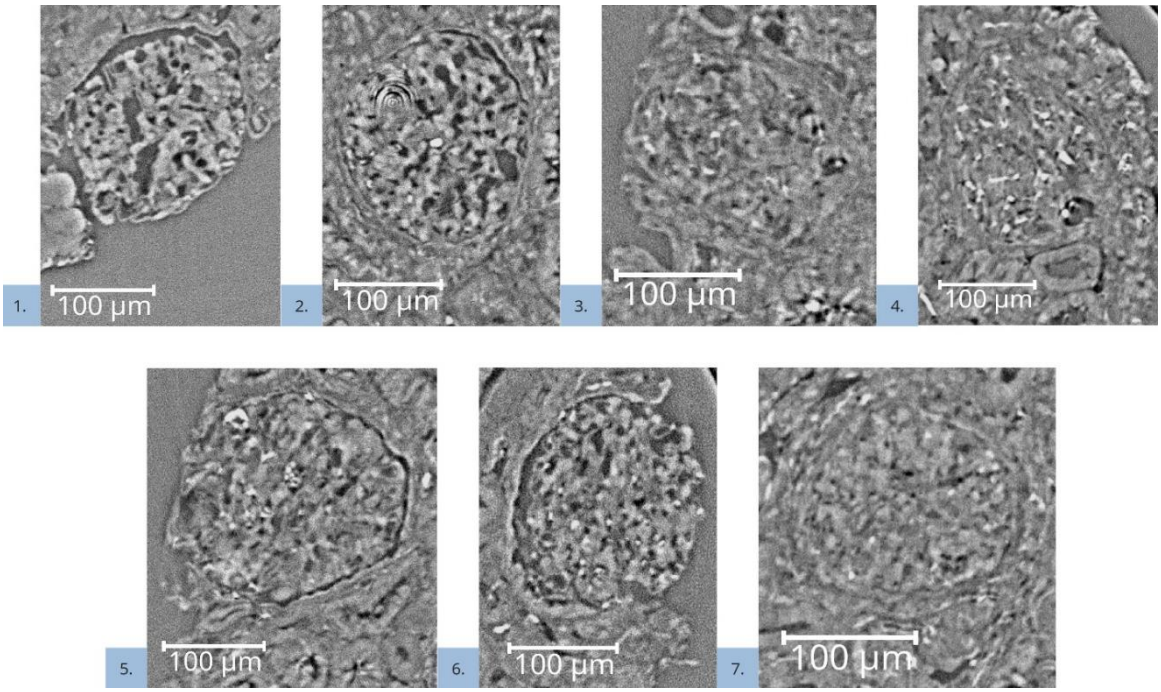

Figure 29: A cross-section of all glomeruli from AMR-low dataset EM04628 in the XY plane numbered according to their index
Glomeruli 1, 2, 4, 5 and 6 are open. Glomerulus 3 is globally and glomerulus 7 is segmentally sclerosed.
AMR – antibody-mediated rejection

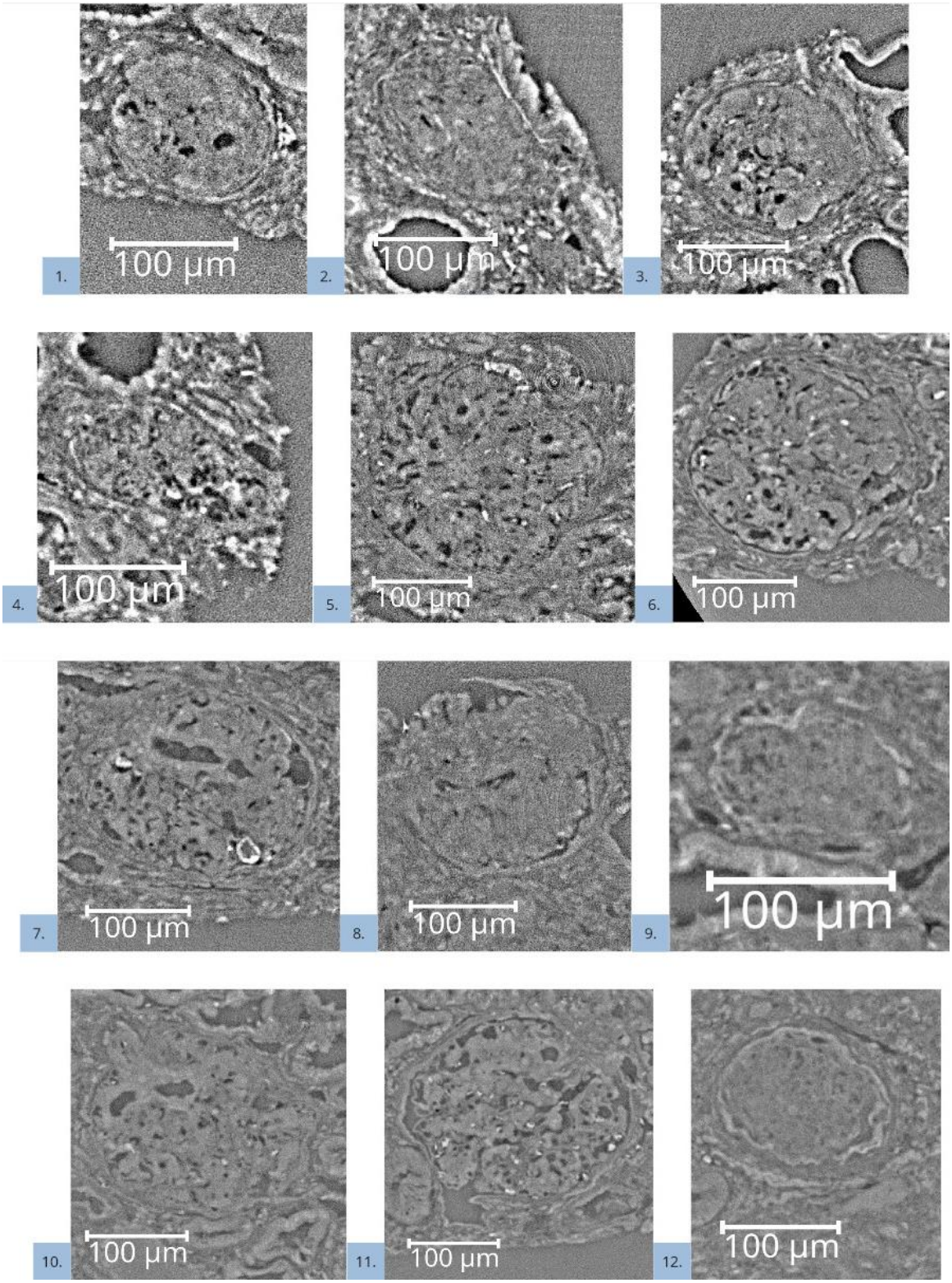

Figure 30: A cross-section of all glomeruli from DSAneg dataset EM04633_2 in the XY plane numbered according to their index
Glomeruli 4 and 11 are open. Glomerulus 12 is globally sclerosed. All other glomeruli are segmentally sclerosed.
DSAneg – donor-specific antibody negative

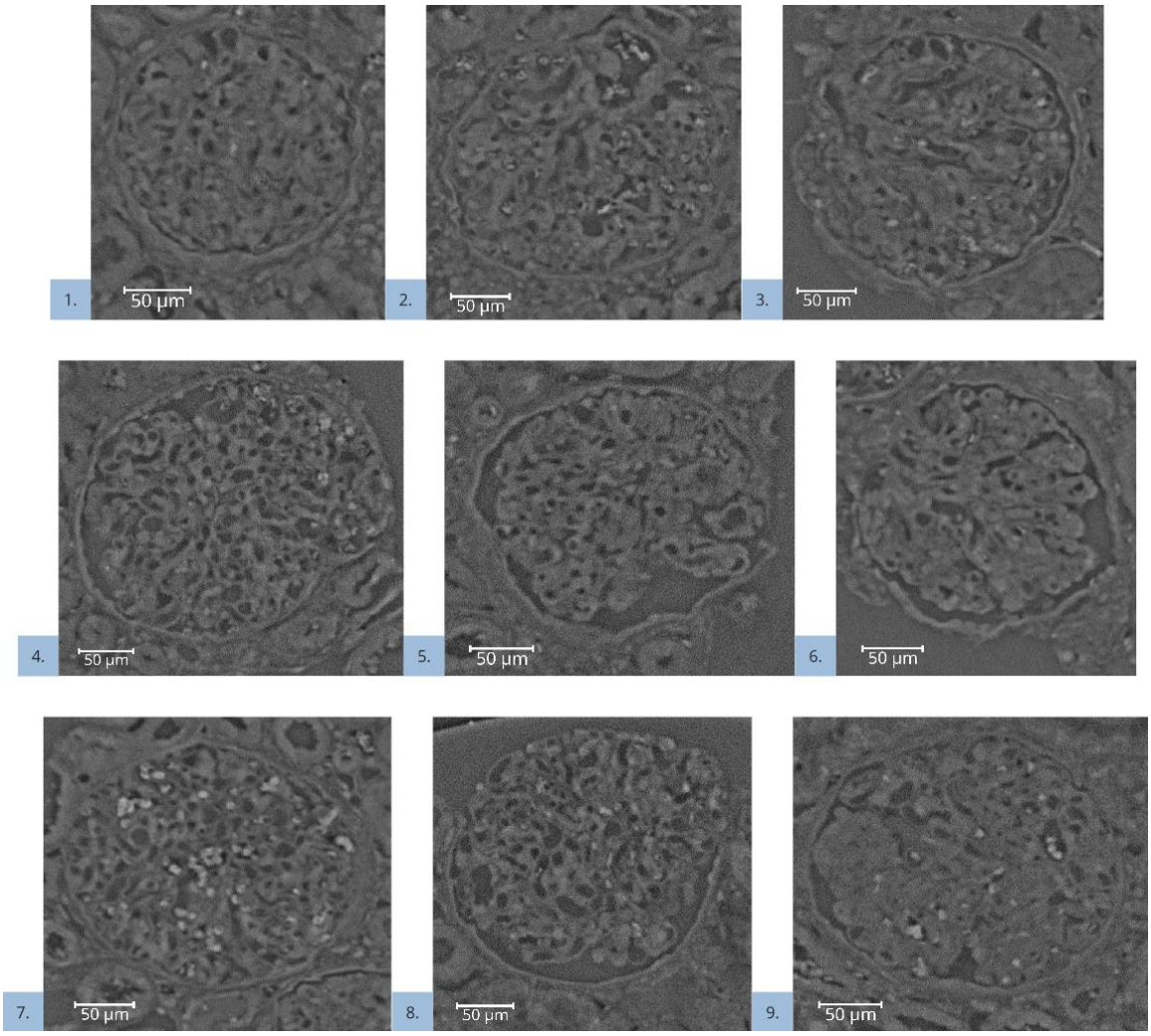

Figure 31: A cross-section of glomeruli 1-9 from DSAneg dataset EM04639_1 in the XY plane numbered according to their index
Glomeruli 1-8 are open. Glomerulus 9 is segmentally sclerosed.
DSAneg – donor-specific antibody negative

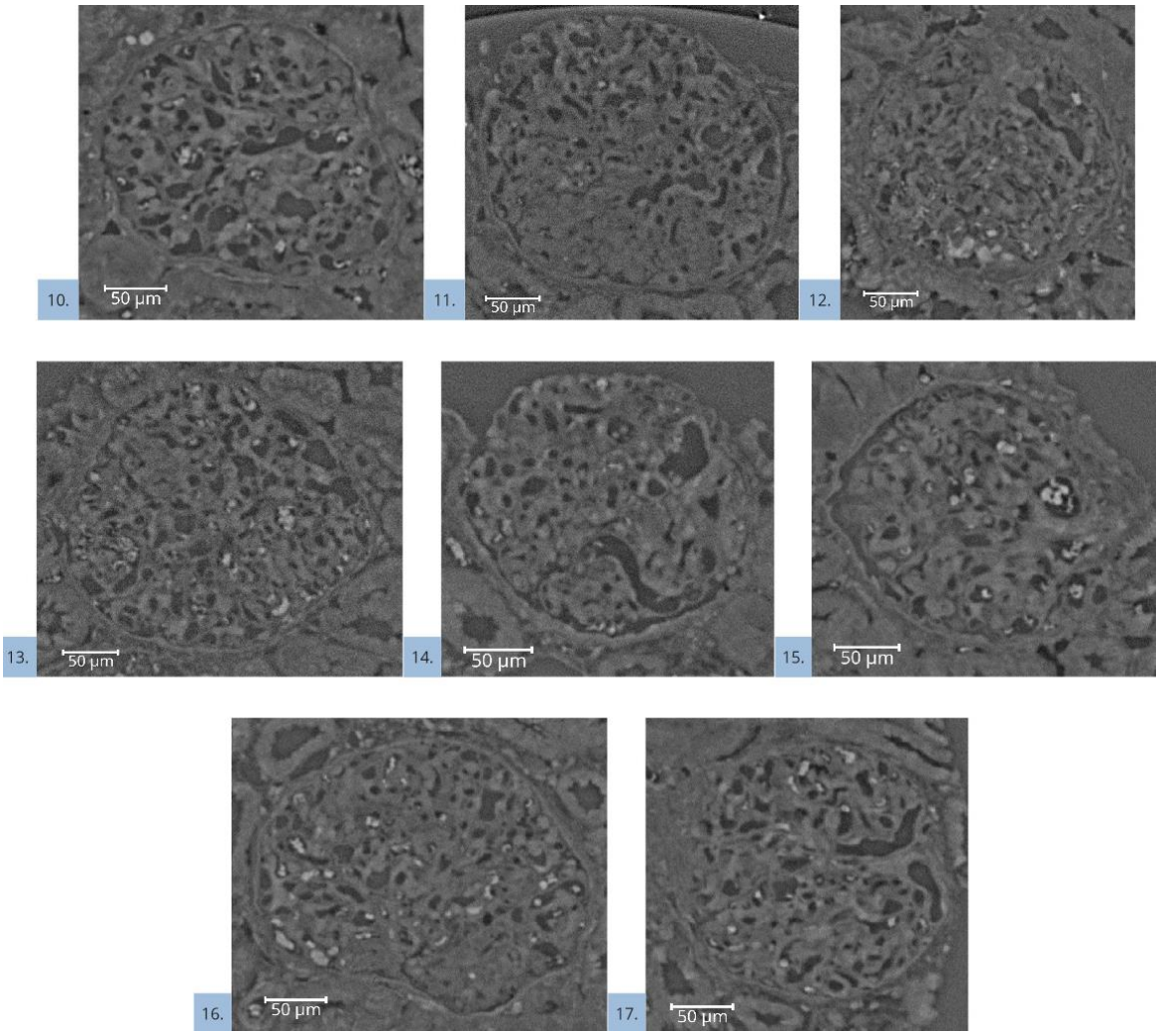

Figure 32: A cross-section of glomeruli 10-17 from DSAneg dataset EM04639_1 in the XY plane numbered according to their index
Glomeruli 10-11 and 13-17 are open. Glomerulus 12 is segmentally sclerosed.
DSAneg – donor-specific antibody negative

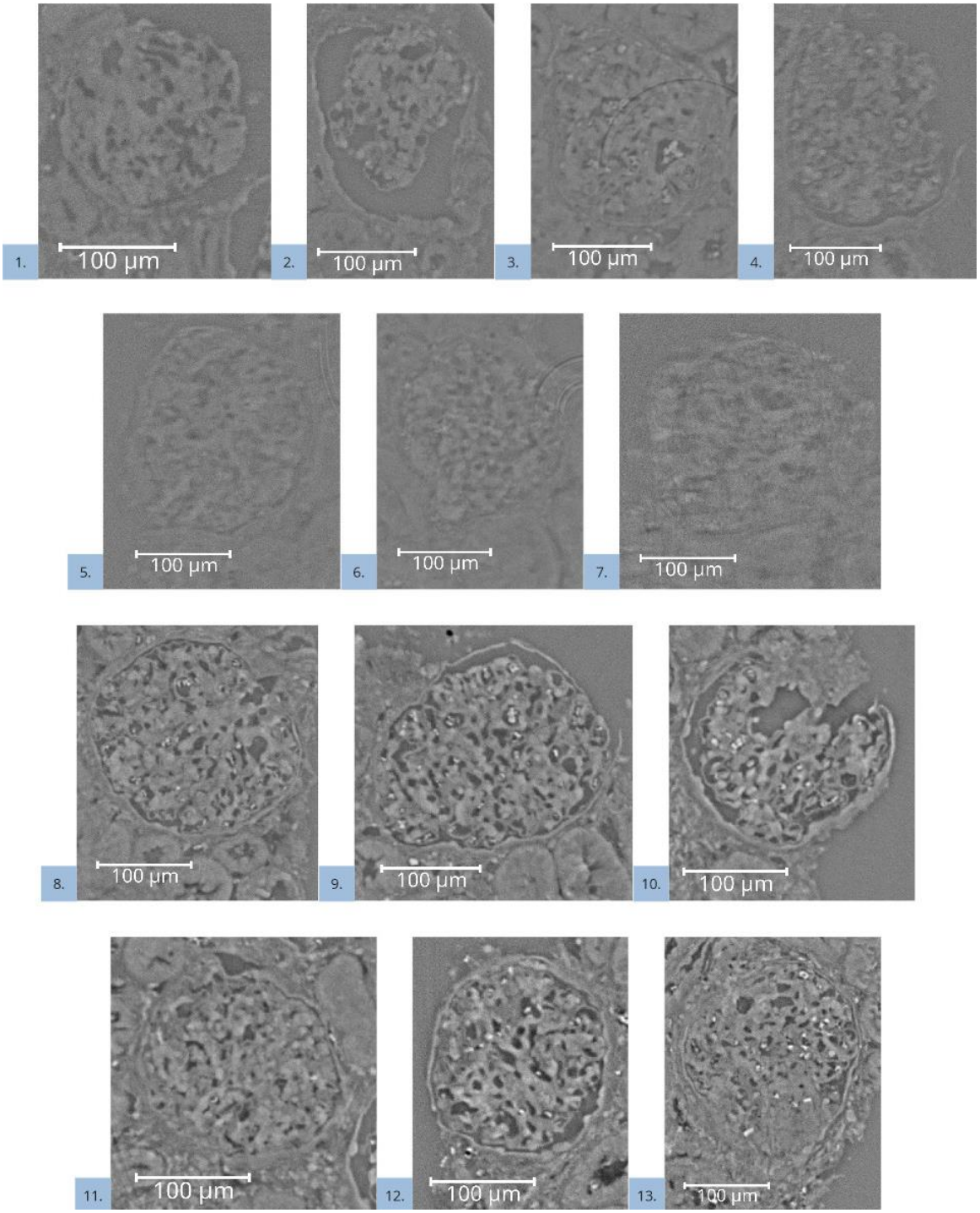

Figure 33: A cross-section of glomeruli 1-13 from AMR-low dataset EM04657_2 in the XY plane numbered according to their index
Glomeruli 1-10 and 12 are open. Glomeruli 11 and 13 are segmentally sclerosed.
AMR – antibody-mediated rejection

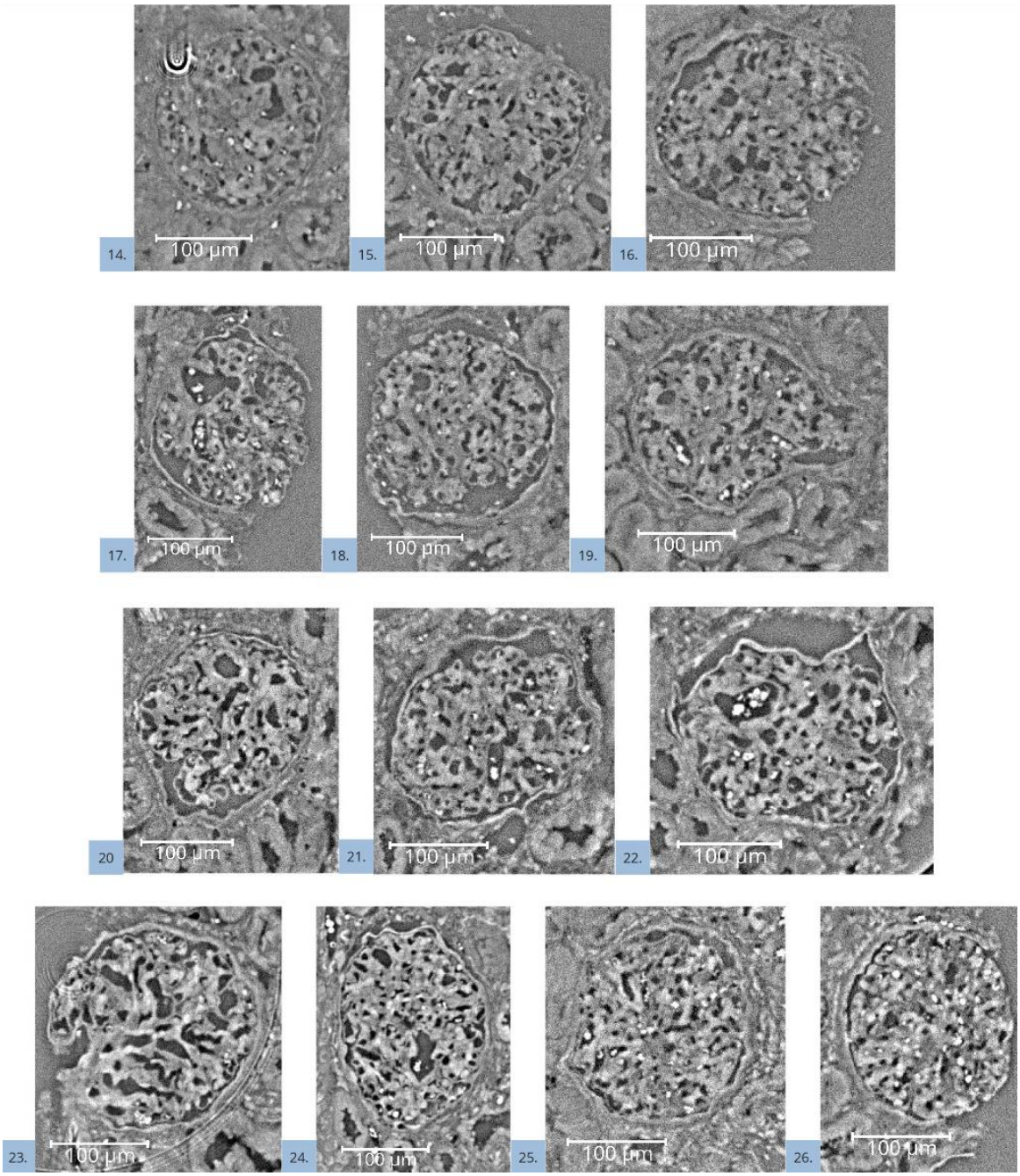

Figure 34: A cross-section of glomeruli 14-26 from AMR-low dataset EM04657_2 in the XY plane numbered according to their index
Glomeruli 14-26 are open.
AMR – antibody-mediated rejection

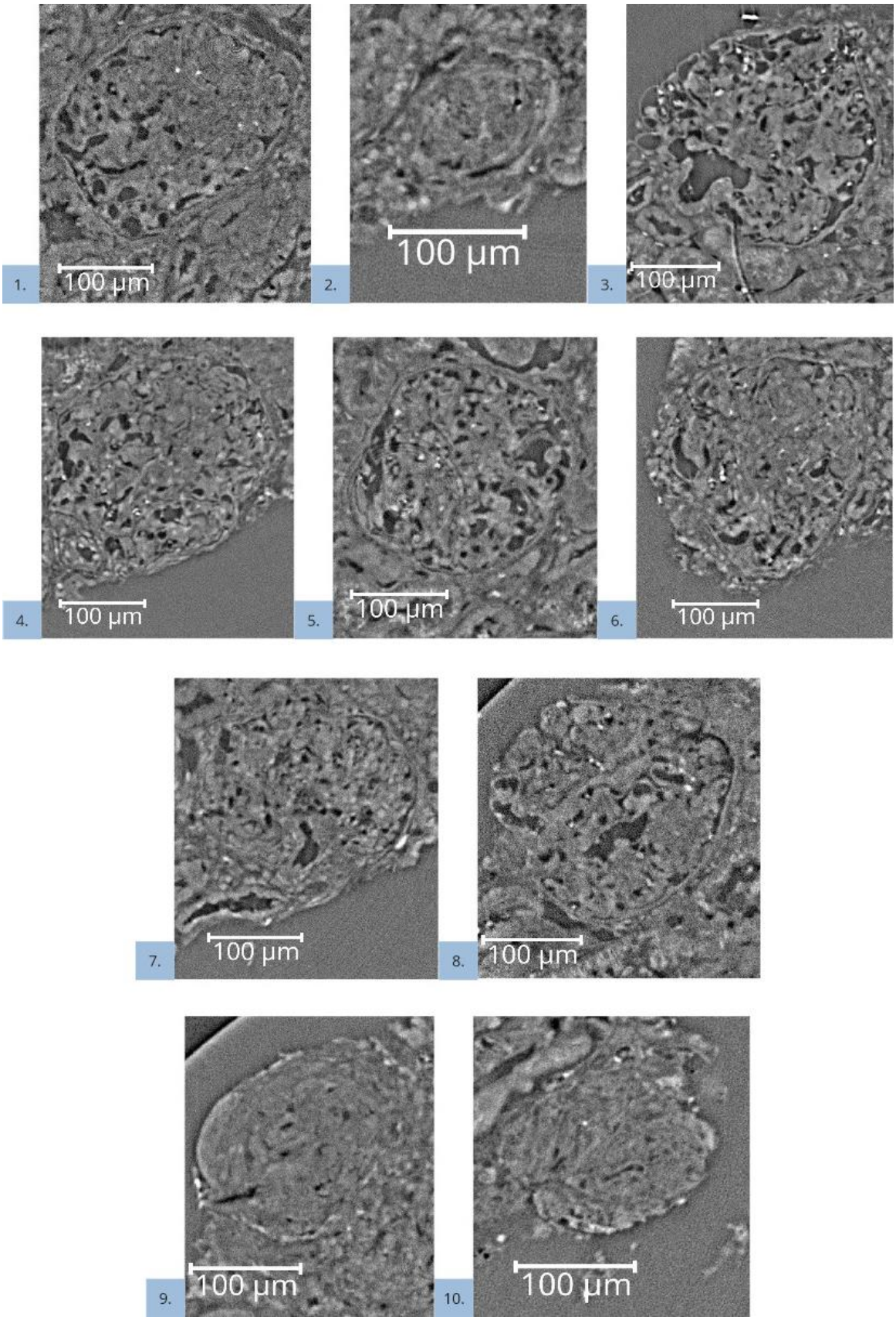

Figure 35: A cross-section of all glomeruli from AMR-high dataset EM04691_2 in the XY plane numbered according to their index
Glomeruli 2, 9 and 10 are globally sclerosed. All other glomeruli are segmentally sclerosed.
AMR – antibody-mediated rejection